Available on CMS information server

CMS NOTE-2008/014

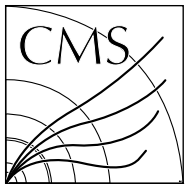

The Compact Muon Solenoid Experiment

CMS Note

Mailing address: CMS CERN, CH-1211 GENEVA 23, Switzerland

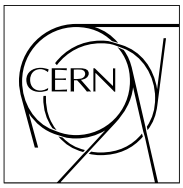

16 July 2007

The 2003 Tracker Inner Barrel Beam Test

T. Boccali[1)], A. Bocci[2)], L. Borrello[1)], E. Carrone[3)], M. Chiorboli[4)], V. Ciulli[2)], C. Civinini[2)], M.R. D'Alfonso[1)], N. De Filippis[5)], R. Dell'Orso[1)], F. Drouhin[6)], S. Dutta[1)], A. Giammanco[1)], A. Giassi[1)], D. Giordano[5)], A. Kaminsky[7)], A. Macchiolo[2)], C. Marchettini[2)], M. Meschini[2)], L. Mirabito[3)], S. My[5)], F. Palla[1)], F. Palmonari[1)], S. Paoletti[2)], V. Radicci[5)], R. Ranieri[2)], G. Segneri[1)], P. Siegrist[3)], L. Silvestris[5)], A. Tricomi[4)], A. Tsirou[3)], P.G. Verdini[1)]

Abstract

Before starting the CMS Silicon Strip Tracker (SST) mass production, where the quality control tests can only be done on single components, an extensive collection of activities aiming at validating the tracker system functionality has been performed. In this framework, a final component prototype of the Inner Barrel part (TIB) of the SST has been assembled and tested in the INFN laboratories and then moved to CERN to check its behaviour in a 25 ns LHC-like particle beam. A set of preproduction single-sided silicon microstrip modules was mounted on a mechanical structure very similar to a sector of the third layer of the TIB and read out using a system functionally identical to the final one.
In this note the system setup configuration is fully described and the results of the test, concerning both detector performance and system characteristics, are presented and discussed.

[1)] INFN and University of Pisa and SNS, Pisa, Italy

[2)] INFN and University of Firenze, Firenze, Italy

[3)] CERN, Geneva, Switzerland

[4)] INFN and University of Catania, Catania, Italy

[5)] INFN and Dipartimento Interateneo di Fisica, Bari, Italy

[6)] University of Mulhouse, Mulhouse, France

[7)] INFN and University of Padova, Padova, Italy

1 Introduction

In order to verify the basic functionalities of the Tracker Inner Barrel (TIB) of the CMS Silicon Strip Tracker (SST) [1] before starting the mass production, a number of activities of increasing complexity has been carried out on detector structures. In this framework, after the prototyping phase, a sector similar to the third TIB layer has been assembled using final production components as soon as they became available.
These activities, also known under the name of "system tests", were initially carried out in laboratory with the main goal of studying the system capabilities in terms of readout performance and noise behaviour. In a second phase, the TIB layer 3 prototype has been exposed, together with a set of Tracker Outer Barrel (TOB) silicon microstrip modules and a Tracker End Cap (TEC) structure ("petal"[1)]), to a 25 ns beam in order to study its response to minimum ionizing particles bunched in a LHC-like time structure. The description of this test, carried out at the X5 test beam facility [2] of the SPS accelerator at CERN, and the results obtained are the subject of the present note.
In the following, after an introduction to the SST layout, sensors and electronics, the beam test setup will be described in detail, with special attention to the TIB shell configuration, silicon microstrip modules, readout, slow controls and power supplies. The data analysis methods will then be summarized and the main test results presented and discussed.

2 The CMS Silicon Strip Tracker

2.1 Detector layout

The CMS SST instruments the range between 20 cm and 116 cm in radius and $\pm$ 280 cm in z [2)] around the LHC interaction point. The pseudorapidity (η) coverage is $|\eta| < 2.5$. The central region ($|z| < 118$ cm) is split into an Inner Barrel (TIB), comprising four detector layers, and an Outer Barrel (TOB), which has six layers. The TIB is shorter in $|z|$ than the TOB, and is complemented by three Inner Disks per side (TID), each disk being in turn composed of three rings. The forward and backward regions (124 cm $< |z| <$ 282 cm) are covered by nine Endcap (TEC) disks per side, each comprising up to seven rings. The two innermost layers of both TIB and TOB as well as rings one, two and five of TEC and one and two of TID are instrumented with double-sided modules. For a complete description of the silicon tracker layout (Fig. 1) see [3].

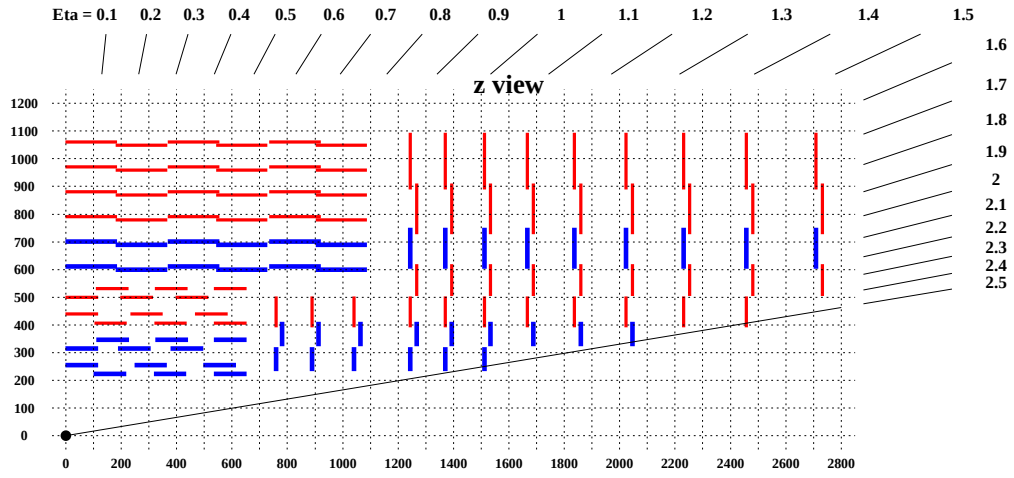

Figure 1: Longitudinal cross section of one quarter of the CMS SST. Thicker (blue) segments indicate double-sided silicon microstrip modules. The nominal beam interaction point is located in (0,0); dimensions are in mm. The pseudorapidity (η) coverage is also shown.

The whole tracker region is embedded in the CMS 4 Tesla solenoidal magnetic field. A transverse momentum resolution of about 1.5% for centrally-produced muons of 100 GeV/c is expected [4].

[1)] A petal is a modular structure which holds detectors and services for a sector of an end cap disk.

[2)] z is the coordinate along the LHC beam axis.

2.2 The TIB silicon strip modules

The silicon strip module design has been kept as simple as possible to ease the mass production and integration procedures. A TIB single-sided module is assembled from the following components: a carbon fiber support frame, a silicon microstrip sensor, the front-end multilayer Kapton hybrid, with a strip pitch adapter glued onto it, and a Kapton printed circuit carrying the bias to the sensor whilst providing electrical insulation from the conductive carbon fiber support frame. All these components pass a chain of mechanical and/or electrical quality tests before being assembled in a module.
Figure 2 shows a single-sided TIB module identical to the ones used during the beam test.

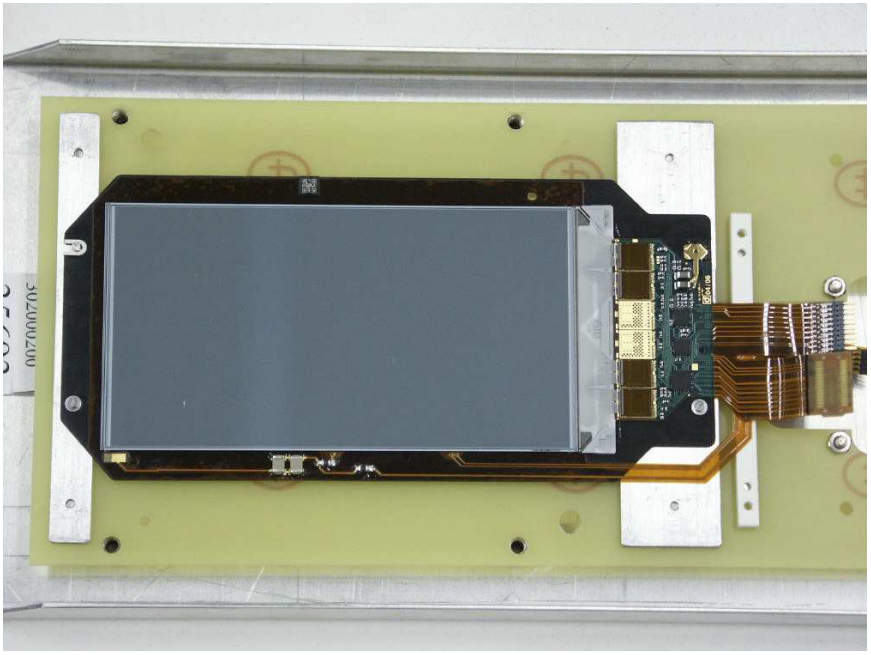

Figure 2: A TIB single-sided module fixed on its transportation cradle.

The TIB modules have a strip length of approximately 12 cm and pitch of 80 μm (double-sided, 768 strips per module) and 120 μm (single-sided, 512 strips per module). These detectors are produced from individual, 320 μm thick, sensors.
All silicon strip sensors [5, 6] are of the single-sided type[3)]. Double-sided TIB detectors are built by simply assembling two independent single-sided modules ("R-Phi" and "Stereo") back to back. To obtain a coarser but adequate resolution on the longitudinal coordinate the stereo module has the sensor tilted by 100 mrad[4)] with respect to the R-Phi module. The stereo sensor and electronics are identical to the R-Phi ones, the only difference being in the support mechanics and pitch adapters.
The module assembly is done automatically using a "gantry" pick and place machine [7, 8].The main steps are the following: the Kapton printed circuit is glued onto the carbon fibre frame, and then the sensor is glued in a precisely defined position on this support, making use of the precision reference marks present on the sensor and of the precision aluminium inserts located on the frame. These inserts will later define the position of the individual module with respect to the mechanical structure of the tracker and therefore to the reference coordinate system of the experiment. Finally, the front-end hybrid and the pitch adapter are glued on the frame; in this case the precision required is less stringent, being imposed only by the requirements of bondability of the sensor to the pitch adapter, and, in case of double-sided modules, by the tracker support mechanical clearance.
The module readout strips and the bias and ground lines are then wire-bonded to the corresponding pads. After

[3)] The SST sensors are of "p-on-n" type with integrated decoupling capacitors, aluminium readout strips and polysilicon bias resistors.

[4)] Greater stereo angles would improve the z resolution at the expense of an greater increase in the "fake hit" rate with the particle density.

these steps, the module undergoes a chain of tests both at room (20 °C [9]) and operating temperature (-15 °C) to identify all possible defects.
The tracker microstrip sensors have been designed on the basis of the results of extensive research and development activities [10] to obtain detectors able to survive the LHC radiation environment for at least ten years of operation [5]. An efficient cooling system is very important to reduce the radiation damage effects on the silicon sensors and to remove the power dissipated by the front-end electronics. For these reasons the CMS silicon tracker has a cooling system which uses a coolant (Perfluorohexane, C_6F_{14}) at a temperature of -20 °C or below. This in turn puts more stringent requirements on the behaviour of the modules under stress induced by temperature variations.

2.3 Silicon strip tracker electronics

A scheme of the silicon strip tracker readout electronics is shown in Fig. 3. The signals coming from each strip are processed by front-end readout chips (APV25 [11]) mounted on a multilayer Kapton hybrid circuit.

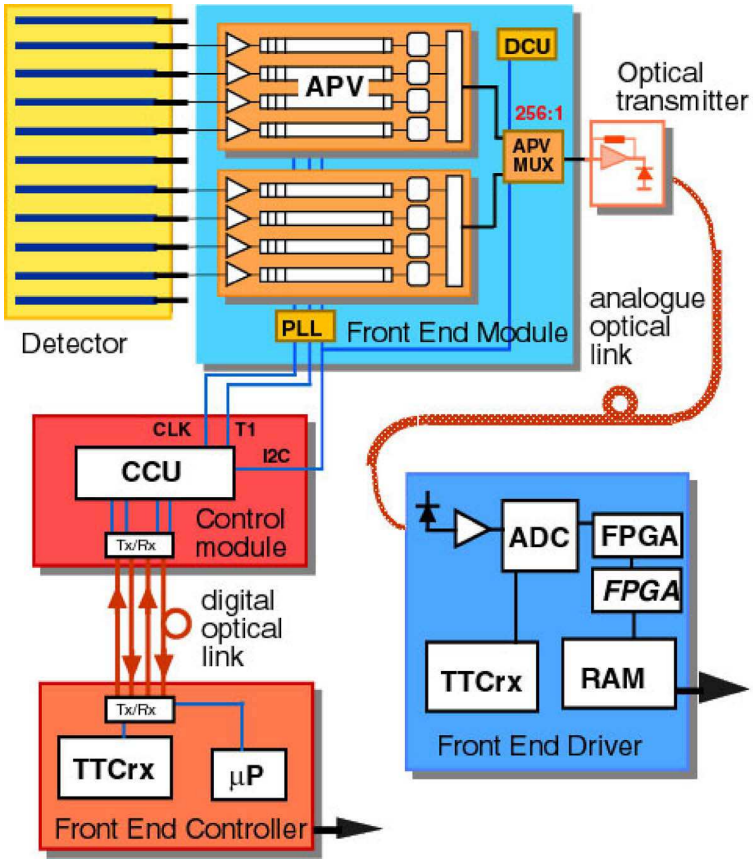

Figure 3: Scheme of the tracker readout architecture.

The APV25 is a 128 channel chip built in 0.25 μm CMOS technology. The thin gate oxide together with special layout techniques ensure its radiation tolerance [12]. Each channel consists of a charge-sensitive preamplifier coupled to a shaping stage which produces a 50 ns CR-RC pulse shape. The output of each shaper channel is sampled at 40 MHz and held in a 192 cell deep analogue pipeline. This pipeline depth allows for a programmable level 1 trigger latency of up to 4 μs, with 32 locations reserved for buffering sample data awaiting readout. Each pipeline channel is read out by analogue circuitry which can operate in one of two modes: in peak mode, only one sample per channel is read (timed to be at the peak of the analogue pulse shape). In deconvolution mode [13], instead, three samples are sequentially read and the output is a weighted sum of all three. The deconvolution operation results in a re-shaping of the analogue pulse shape to one that peaks at 25 ns and returns rapidly to the baseline. This operating mode is particularly important for the correct bunch crossing identification during the high luminosity running phase of the LHC. A unity gain inverter, which also reduces the common mode noise contribution

[5] Equivalent to an integrated luminosity of 500 fb^{-1} or, in the innermost TIB layer, to a fluence of 1.6×10^{14} 1-MeV equivalent neutrons/cm^2 (n_{eq}/cm^2).

by subtracting the common input noise from the output signal, is included between the preamplifier and shaper and can be switched in or out.
On receiving a positive level 1 trigger decision the APV25 outputs serially, at a rate of 20 MHz, the 128 analogue signals corresponding to the beam crossing which originated the trigger, one latency time earlier, together with information about the internal pipeline address and the chip error status; signals coming from two APV25 are interlaced together on a differential line by a multiplexer chip [14] which is mounted on the hybrid circuit very close to the front-end chips. When the APV25 chip is clocked but does not receive any trigger it outputs, every 70 LHC clock cycles, a synchronisation signal, called "tick mark", of about 25 ns duration (after the output of 2 APVs is multiplexed, the corresponding tick mark lasts about 50 ns). This signal can also be used for a rough measurement of the overall gain of the readout chain, as its height represents the full nominal span of the APV output.
The analogue electrical signals are then converted to optical signals in dedicated Analogue OptoHybrids (AOH) [15] located few centimetres away from the silicon microstrip module, and transmitted to the counting room by means of single-mode optical fibres [16], where they are digitized [17]. Each optical fiber carries the analogue signals coming from two APV25 chips through one multiplexer.
By means of such an architecture, the control signals and the analogue data are brought from or to the outside of the tracker using optical fibres which electrically decouple the detector from the readout system and reduce the space and the material needed to connect the instrument to the off-detector electronics.
The LHC 40 MHz clock, which drives the APV25 sampling, is synchronized at the single module level by means of a PLL (phase-locked loop) chip [18]. In this way a signal generated by the passage of a particle can be correctly sampled at its maximum regardless of the module position with respect to the LHC interaction point and of the different clock line delays. The entire readout chain is able to sustain a level 1 trigger rate of about 100 kHz. The functional parameters of the devices located inside the tracker can be uploaded from outside using the I^2C [19] standard communication protocol. They can also be read back from the chips for data integrity check. Finally, a slow parameter control chip (Detector Control Unit or DCU [20]) converts, using an internal 8-channel 12-bit ADC, module temperatures, low voltage levels and high voltage currents making the values available to the main Data Acquisition System (DAQ) via I^2C.

2.3.1 TIB shell electronics

The TIB detectors are assembled into linear structures, called "strings", each made of three modules connected to a Kapton circuit distributing power and control signals ("mother cable") using controlled impedance lines and LVDS buffers for better signal quality. Data are converted to optical levels for remote digitization by means of analogue lasers mounted on the AOH and single-mode (1310 nm) optical fibres.
In the final tracker configuration the opto-electrical conversion and the digitization will both happen on 96 channel VME-9U boards [17] (FED-VME).
A CCU chip [21], directly mounted on the mother cable, decodes the clock and control signals from the digital frames coming from the "Digital Opto-Hybrids" (DOH [22]) which, in turn, convert the optical commands coming from the Front End Controller (FEC) [23] located in the control room. The token-ring structure made by a DOHM (a board used to host the DOH and the routing of the ring lines) and a variable number of CCUs and mother cables, is called a "control ring". The operating parameters of the APV25, PLL, Multiplexer, DCU and AOH can be downloaded and read back using the control ring.

3 The Beam Test Detector Setup

3.1 The TIB shell

The TIB prototype system under test was a portion of the third layer of the Tracker Inner Barrel (Fig. 4). This structure was equipped on the outer side of the cylinder only. Supports for a total of four "strings", all of them fully provided with services, were assembled. As already stated and as shown in Fig. 4, a TIB string is assembled on a longitudinal structure, parallel to the shell axis, which holds the services (opto-electrical connections, cooling and mechanical supports) needed for the three modules. During this test two strings were fully equipped with a total of six modules, in the final configuration. All four strings were under power and received the clock signals, simulating, from the control electronics point of view, a portion of a complete TIB "control ring"[6)].

[6)] In the final TIB Layer 3 a control ring will be made of 15 strings.

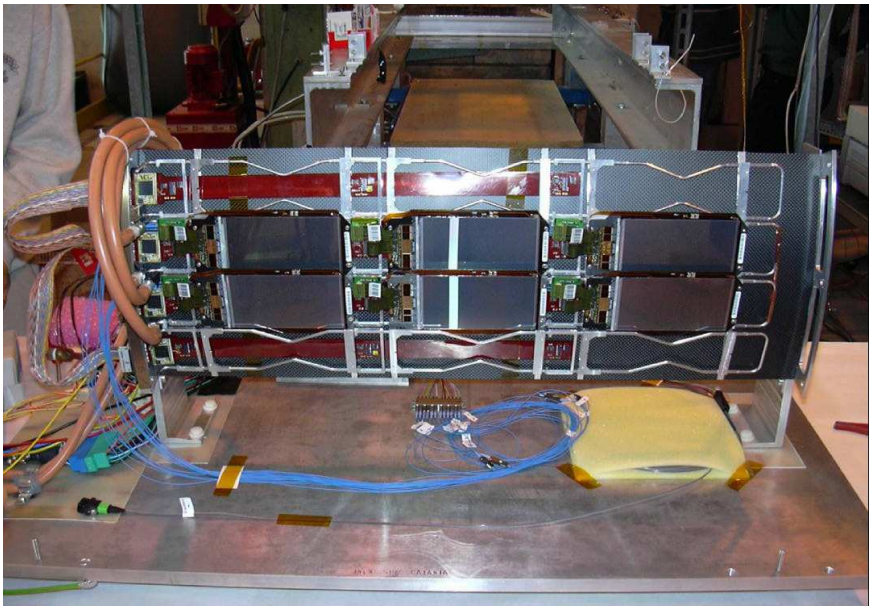

Figure 4: The TIB Layer 3 prototype.

The shell was fully assembled in laboratory and then transported to CERN. For the detector transportation a simple box was used; the only important safety measure needed was to secure all the parts to the structure and mechanically decouple the latter with respect to the box in order to avoid mechanical resonances at dangerous frequencies which could result in damage to the modules. The transport was a test, on a small scale, of the final detector assembly logistics: the TIB layers and TID disks are assembled in different clean rooms in Italy (Florence, Pisa and Turin) and then moved to the main assembly centre (Pisa). Then, when the two TIB-TID full detector halves are ready, they are moved to CERN where they are integrated inside the tracker support tube together with TOB and TEC. The transport, considered as a part of the "system test" itself, was a success: not a single strip was lost.

3.1.1 TIB shell prototype electronics

During this test the analogue optical signals coming from the AOHs were converted back to electrical signals by means of dedicated opto-electrical converters located in the control room, and read out with Tracker PMC ADC boards (FED-PMC [24]). The FED-PMC are mounted on a PCI bus using a standard PCI-PMC adapter.
For this beam test electrical FEC prototypes, also mounted on PCI-PMC adapters, were used. The modules were coupled with dedicated electro-optical converters to optically drive the DOHs. These were located on a special board, different from the final one (DOHM) used on the final TIB-TID detector and not available at the time.
The rest of the detector electronics chain comprises only final or pre-production components.

3.1.2 Power supply system

During the 2003 TIB beam test two prototypes of the CMS tracker power supplies were tested. The two systems were developed by CAEN and Laben respectively, in close contact with the INFN-Florence group.
Both prototypes were designed to work in the counting room located about one hundred metres away from the tracker[7]. During this test both prototypes were used to power the TIB structure through 125 m long connections using a dedicated "low impedance cable" (LIC). An additional floating power supply was used to power the control ring electronics separately.
In this test the power connections were implemented with two versions of the LIC cable, connected in series:

[7] Later developments led to internal modifications of the power supply units, leaving the system architecture unchanged. The aim was to place the power supply system in the experimental cavern, in presence of a residual magnetic field and neutron radiation background. This choice represents a considerable saving both in the capital investment for the cables and in the human resources needed for the cable deployment, at the expense of additional operational risks and maintenance drawbacks.

LIC17, 90 metres long and 17 mm of diameter and LIC11, 35 metres long and 11 mm of diameter. Such a setup allows testing the system configuration in which the power supplies are located outside the CMS cavern: the 90 m cable connects them to a patch panel placed just outside of the CMS apparatus, while the 35 m long cable reaches the PP1 patch panel located inside the detector. The two cable types were also designed to optimize the cable power dissipation while minimizing the material inside CMS.
Each cable consists of the power lines (2.5 V, 1.25 V, common return) of four high voltage pairs plus other services (sense wires, temperature/humidity sensor readout) and is shielded by a copper braid. The LIC cables were specifically developed for the TIB power supplies with the aim both to minimize the inductance and to maximize the capacitance between the power lines. These consist of enamel-insulated copper conductors in close mechanical contact with each other and sense wire pairs are present to allow the regulators of the supply unit to compensate for the voltage drop along the cable.
The common return of power lines and high voltages, the LIC external shield and the CCU ring return were connected together to the X5 experimental area "earth" in a single point, very close to the detectors, and also connected to the TIB mechanical structure. The structure support plate and the external shielding box were instead kept floating.

3.1.3 The TIB mechanics and cooling

The mechanics used to support the modules and the services is visible in Fig. 4. A prototype of a portion of the TIB Layer 3 was assembled in carbon fiber (the layer cylindrical skin) and aluminium (the end flanges and the structure reinforcement elements). In the final tracker most of the structure will be realized using carbon fiber, thus reducing the material budget of the system, but the rest of the services are very similar to those used in this test. Precisely machined aluminium plates, called "cooling ledges", are used as reference positioning elements to which the silicon modules are mechanically connected. The ledges themselves have been glued to the layer structure using a precision mechanical mask to guarantee the requested accuracy. Aluminium pipes are glued below the ledges to carry the refrigerating liquid cooling the front-end and optohybrids and keeping the silicon sensors below -10 °C during operation at LHC to reduce the effects of radiation damage as well as the silicon reverse bias current and to minimize the risk of thermal runaway.
To support the TIB structure an aluminium cradle has been built; this holder can be adjusted to expose the modules at different beam incident angles. Finally, a copper-covered fiberglass-epoxy box has been used to shield the entire setup from external electrical interference and light. To reduce the module temperature variations during the data taking period, the shell cooling circuits were connected to an external chiller circulating coolant (glycolic alcohol) at a constant temperature of 18 °C.

3.1.4 The TIB modules

The six silicon microstrip modules installed on the TIB shell came from the preproduction set, the only differences with respect to the final production modules being in the Kapton hybrid circuit: one of the two connectors has in the meanwhile been reinforced, and the hybrid layout changed to cure a problem which was believed to possibly affect long term reliability. The single-sided modules are assembled starting from the IB2 type, final design [5, 6], silicon microstrip sensors for layers 3 and 4 of the TIB and produced by Hamamatsu Photonics [25].
In Table 1 the main characteristics of IB2 type sensors are reported. Most of these numbers are taken directly from the sensor mask design. Table 2 shows the relative positions of the six modules in the experimental setup and their depletion voltages as measured before their assembly using the sensor C-V characteristics (i.e., the bias voltage value above which the sensor total capacitance does not change further).

3.2 Beam Test Trigger

The trigger system used during the test described in this note was implemented with two plastic scintillators placed downstream of the setup. The coincidence of the signals coming from the two photomultiplier tubes, in addition to the SPS 25 ns beam clock, was used as input either to a TSC [26] (Trigger and Sequencer Card) or to a TTC [27] (Trigger Timing and Control) trigger card system providing both a trigger pattern selector and a FED and APV25 clock line fan-out.

Table 1: Summary of IB2 sensor characteristics.

Parameter	
Overall width (after cutting)	63 288 μm
Overall length (after cutting)	118 961 μm
Active area width	61 500 μm
Active area length	116 885 μm
Strip length	116 823 μm
Width of strip p+ implant	30 μm
Pitch	120 μm
Number of strips	512
Width of metal strip	40 μm
Silicon thickness	320 μm
Silicon crystal orientation	$< 100 >$

Table 2: Individual module position on the Layer 3 prototype structure (as seen from the beam line) and depletion voltage of each sensor. The names (TIBn) are the same used to identify the modules in Sect. 6.

String #1	-	-	-
String #2 Depl. Voltage [V]	Mod. TIB1 183.8	Mod. TIB2 183.4	Mod. TIB3 190.8
String #3 Depl. Voltage [V]	Mod. TIB4 188.0	Mod. TIB5 137.9	Mod. TIB6 143.5
String #4	-	-	-

3.3 TOB and TEC setup

Downstream of the TIB two additional SST substructures were present. The first was a thermally insulated box containing six TOB modules with the strips oriented vertically. The second was a partially equipped TEC petal.

4 Data Acquisition System and Interlocks

4.1 DAQ software

The XDAQ [28] architecture was used to control the various data acquisition components. The main part of the system is based on the Event Builder, which reads data from the FED and assembles them in an event structure. The events are then sent to an application which writes a ROOT [29] tree for storage or sends them to a monitoring system.

4.2 DAQ electronics

The beam test readout system was composed by three parallel chains (TIB, TOB and TEC) each one composed of:

- one PC with one TSC and two (or three) FED boards;
- a second PC with a FEC (and an external opto-FEC which converts the FEC electrical signals into optical ones and vice-versa) and a mass storage unit.

The individual subsystem integration, performed according to the following procedure, proved easy. First an I^2C scan of the control ring was done, checking that all the devices present in the system responded correctly. Subsequently, the FED ADC sampling point was individually tuned for each module, synchronizing it with the LHC clock, and the optical gain and bias of all AOH was adjusted. Neither operation required the presence of beam particles, since they rely on the measurement of the APV25 tick marks: the sampling point should be on the

flat top of the tick mark, and the AOH functional parameters are adjusted until the proper gain, in a linear working region of the electro-optical converter, is obtained (for details about this procedure see Sect. 6.2). Finally, using the 25 ns structured beam, a latency scan was performed in order to identify the trigger position in time; this was followed by a PLL scan to refine the sampling: the chosen point in latency and PLL delay is the one that maximizes the total cluster charge collection for each silicon microstrip module.
Once independently commissioned, the TIB and TOB detectors were then read out synchronously. This integration was also performed in a rather short amount of time despite of the fact that the two subsystems have different control rings and that the optical fiber lengths differed by up to 15 metres.
Up to 2500 events per SPS spill[8)] were read out, corresponding to a data rate of about 20 Mb per spill. Limitations to this rate were mainly due to the ROOT compression algorithm performance.

4.3 Slow control system and interlocks

Throughout the beam test, the temperature and the relative humidity inside the detector volumes were monitored almost continuously. In addition, an interlock system was installed and kept the detectors under test protected from potentially dangerous environmental conditions (such as excessive temperature, or the risk of condensation, or rapidly variable conditions).
Another requirement was to protect the devices against the possibility of blackouts of the mains AC power: an Uninterruptible Power Supply (UPS) afforded the short time margin necessary for an orderly ramp-down of the low-voltage power on the front-end electronics and of the high-voltage bias on the sensors.
A human-machine interface program was provided for the visualization of the instantaneous values of the monitored quantities and of their recent history. All values were timestamped and committed to permanent storage for future access.

4.3.1 Temperature sensing

For the temperature measurements, specially calibrated thermistors from Fenwal, similar to the ones that will be installed permanently within the tracker volume, were used. Ad-hoc electronic circuitry was developed to provide proper conditioning for these sensors and produce signals compatible with the industry-standard Programmable Logic Controller (PLC), belonging to the Siemens S7 family, supervising the environmental measurements and implementing the interlock logic.
A partial history of the temperature of the gas filling the TIB box is shown in Fig. 5. A second thermistor, not shown here, was placed on the detector cooling pipe, monitoring the inlet coolant temperature.

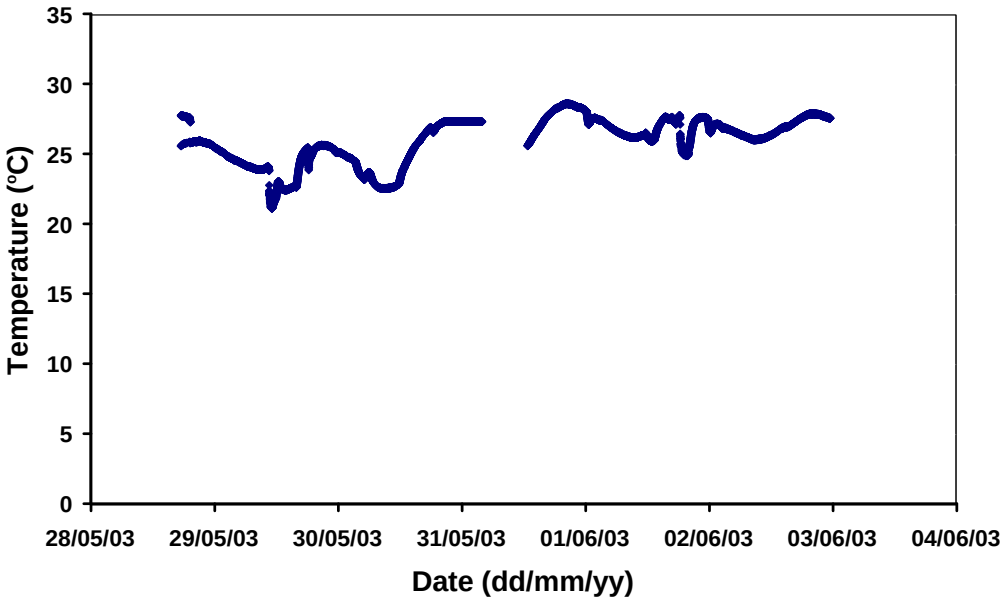

Figure 5: Temperature history for the gas inside the TIB volume

[8)] During the 25 ns LHC-like beam operation the SPS cycle length was 21.6 s with an extraction duration (spill) of 2.2 s.

The interruptions in this and in the following relative humidity plot were caused by a scheduled upgrade of the software running on the PLC and of the visualization program. Since every data point is accompanied by a timestamp, it is very easy to correlate the variations in the sensor dark currents with the environment temperature.

4.3.2 Humidity sensing

For the beam test described in the present paper, a temporary solution to monitor the setup relative humidity, not suitable for operation under the LHC conditions but acceptable for the present application, was found in the Honeywell HIH-3605B sensors [30]. These sensors include active components that are used to convert the relative humidity to a voltage signal which is compatible with the standard analogue inputs of the PLC used. Figure 6 shows the history of the relative humidity measured close to the gas inlet of the TIB volume.

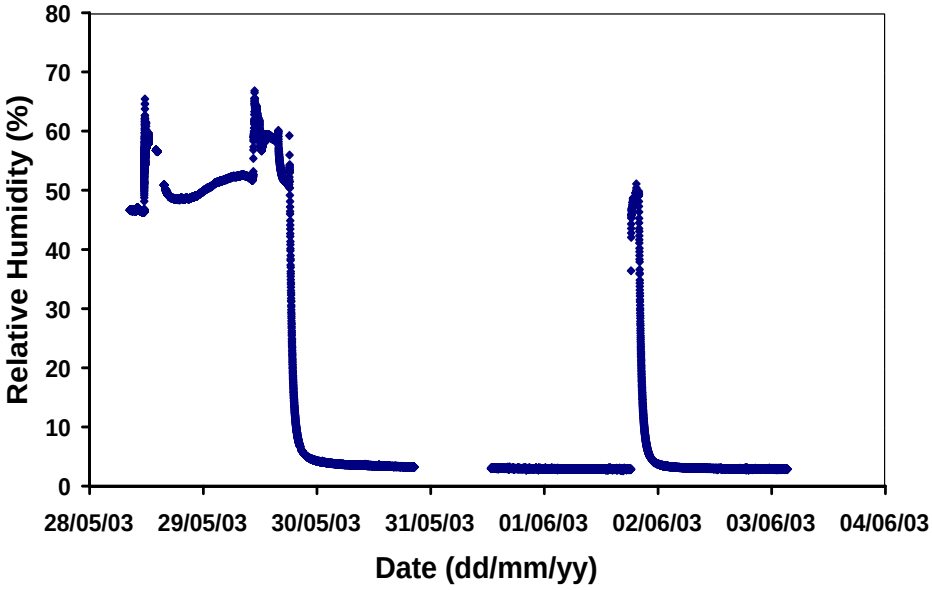

Figure 6: Relative humidity at the TIB gas input.

The period over which the relative humidities are plotted is the same as for the temperatures. Starting on the evening of May 29^{th}, the TIB was flushed with dry nitrogen, apart from a rapid intervention which required breaching the volume gas-tightness on the late evening of June 1st. During the initial period without dry gas flow, the influence of the weather conditions on the relative humidity and temperature within the TIB volume can be seen. On the contrary, when the dry nitrogen is flushed the relative humidity is stable below 5%.

5 X5 LHC-like 25 ns Beam

The X5 [2] SPS beam line at CERN can deliver to the users pion and muon beams of momentum in the range between 5 and 250 GeV/c. During this test we used a low intensity muon beam ($\sim 10^3$ particles cm^{-2}s^{-1}) or a high intensity pion beam ($\sim 10^5 \div 10^6$ particles cm^{-2}s^{-1}), in both cases with 120 GeV/c momentum. This beam comes from the H3 secondary beam generated from the interaction products of the main extracted SPS proton beam on the T1 primary target. During the normal SPS operation particles arriving at the test area are unbunched, with an almost flat time distribution inside the 2.2 s spill time. The spill follows the CERN proton accelerator complex cycle and it is repeated every 21.6 s.
To test the LHC detectors and electronics in a condition similar to the real experiment, the SPS proton beam has been modified to have a 25 ns bunch time structure [2]. Since the SPS has no 40 MHz radio-frequency cavities, the bunched beam was prepared in the PS, quickly injected into the SPS at 26 GeV/c and then accelerated to 450 GeV/c. A PS bunch train of 48 packets, for a full duration of 1.2 μs, was injected into the SPS every 23 μs (SPS orbit period). After acceleration to 450 GeV/c the protons were extracted keeping the same time structure, namely 48 bunches at 40 MHz every 23 μs during the entire 2.2 s flat top duration, and sent to the primary target. A single bunch time width was determined by the 200 MHz SPS accelerating cavity frequency, resulting in about

5 ns. The beam intensity was regulated in such a way to have an occupancy of about one particle or less per bunch ($\leq 2 \times 10^6$ particles/s).

6 Beam Test Data Analysis

6.1 Data analysis methods

The particle signal is extracted from the FED-PMC digitized strip charge (raw data) by subtracting the strip pedestal and the common mode contribution. The latter quantity represents the joint shift of the baseline in a group of contiguous strips (32 in the present analysis) situated on the same APV25 and is computed event by event using an iterative trimmed median algorithm to avoid spurious contributions from either particle signals or noisy strips. The pedestal of each strip is defined as the average of the raw data for that channel. For the purpose of pedestal calculation events where the strip may have been hit by a particle have also been discarded. The strip noise is computed as the root mean square deviation of each APV25 channel with respect to its pedestal value after subtraction of the 32-strips common mode contribution (CMS or Common Mode Subtracted noise). For this test the pedestal, CMS noise and common mode, is calculated offline; in the final experiment these quantities will be computed on board by the FED-VME. The strips are identified as bad (noisy, disconnected or shorted) when the associated noise value is outside an acceptance range; as soon as they are flagged as noisy strips are excluded from further analysis.
In order to identify the passage of a particle, the offline search algorithm computes the signal and noise of each strip according to the previous definitions and looks for clusters of adjacent strips which have a statistically significant charge excess. Initially, the clustering algorithm searches for "seed" strips, defined as those having a signal-to-noise ratio (R) that satisfies $R > T_1$. Once at least one such strip is found, all adjacent strips having $R > T_2$ are added to the cluster. When no more adjacent strips above threshold are found, the total cluster charge S_C is computed as the sum of the pulse heights over the accepted strips. The cluster noise is then computed as $N_C = \sqrt{\Sigma_i N_i^2 / L_C}$ where N_i is the noise of strip i and L_C the number of strips accepted for that cluster. If the condition $S_C/N_C > T_3$ is not satisfied, the cluster is discarded. The hit position is calculated for each accepted cluster as the pulse height-weighted mean ('centre-of-gravity') of the cluster strip locations. For the present analysis, the values used for the cuts are the following: $T_1 = 4$, $T_2 = 3$ and $T_3 = 5$.

6.2 Analogue optohybrid gain scan and signal normalization

After the DAQ system has been configured for data taking the AOH settings must be tuned in order to have the lasers operating in the linear region with a correct gain. This procedure is part of the DAQ program and it is executed upon operator request. If the system is kept stable, for example the optical connections are properly handled and the temperature does not change dramatically, this procedure only needs to be run once, at the beginning of data taking.
The AOH laser parameters are accessible through the "gain" and "bias" I^2C registers of the linear laser driver chip [31]: the former accepts integer values between 0 (low gain) and 3 (high gain) while the latter regulates the laser diode bias current which can be trimmed over the range 0-55 mA (corresponding to register values between 0 and 60), to set the laser in the linear region of operation.
During this process the DAQ program sends clock signals, but no triggers, to each APV25 in order to have continuous tick mark digitization at the FED. For each "gain" setting a "bias" scan is performed, with the DAQ software computing the tick mark base (called "digital 0"), its high level or "tick" ("digital 1") and the difference. The optimal point is chosen so as to maximize the difference (Fig. 7) while keeping the two digital levels very close to the extreme values of the AOH linear range (Fig. 8) but not saturated. The value for the gain register is chosen in such a way that the optical chain overall amplification is close to 0.8V/V [32].

The analogue optical signal reaches the opto-electrical converter, before entering the FED, via ~ 100 m of optical fibre with three optical connections. Therefore, the relative gain of each optical chain could in principle be different, mainly because of the possibility of a less than optimal optical contact at the connectors but also because of laser gain non-uniformities and temperature induced shifts. Hence the output signal of different of APV25 pairs, which are multiplexed on different fibres, should be normalized to a reference value in order to compare their pedestal, noise and cluster charge values. The ADC raw values are normalized for each run by forcing the tick mark height (digital 1 - digital 0 difference) to an arbitrary chosen value of 230 ADC counts. Table 3 shows the normalization factors for each APV25 pair of the six TIB detectors for a typical run. It is important to note that, if the laser works in a linear region, relative quantities, for example signal-to-noise ratios, are not affected by gain variations.

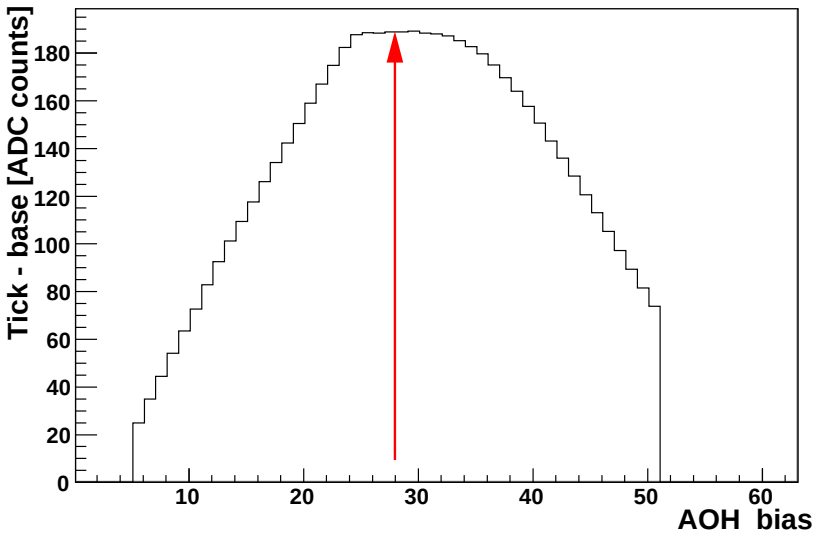

Figure 7: Tick-base difference vs. bias (register setting) for one AOH channel (gain = 1). The vertical arrow indicates the optimum point selected by the DAQ software (bias = 28).

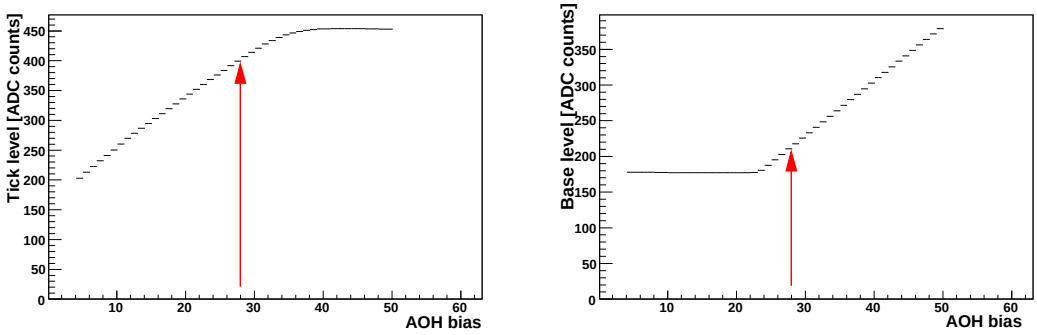

Figure 8: Tick (left) and base (right) levels (ADC counts) vs. bias (register value) for the same AOH channel of Fig. 7 and the same gain. The vertical arrows indicate the optimum point selected by the DAQ program (bias = 28).

Due to the different gain of the optical chains, the profile of the common-mode subtracted noise profile normally

Table 3: Examples of optical normalization factors used during this analysis. The higher values (around 1.5) shown for some cases reflect different "gain" settings for these channels.

	Normalization factor	
Module	AOH 1	AOH 2
TIB1	1.52	0.89
TIB2	1.16	1.05
TIB3	1.14	0.98
TIB4	1.13	1.22
TIB5	1.00	1.49
TIB6	1.12	0.83

shows a distinct step at the transition from the first APV25 pair of the module to the second. After the AOH normalization factors are applied the noise profile flattens (Fig. 9). Figure 10 shows the optical chain gains, run by run. The gains are stable during data taking unless the optical fibres are disconnected and reconnected. All data reported in section 7 come from renormalized data.

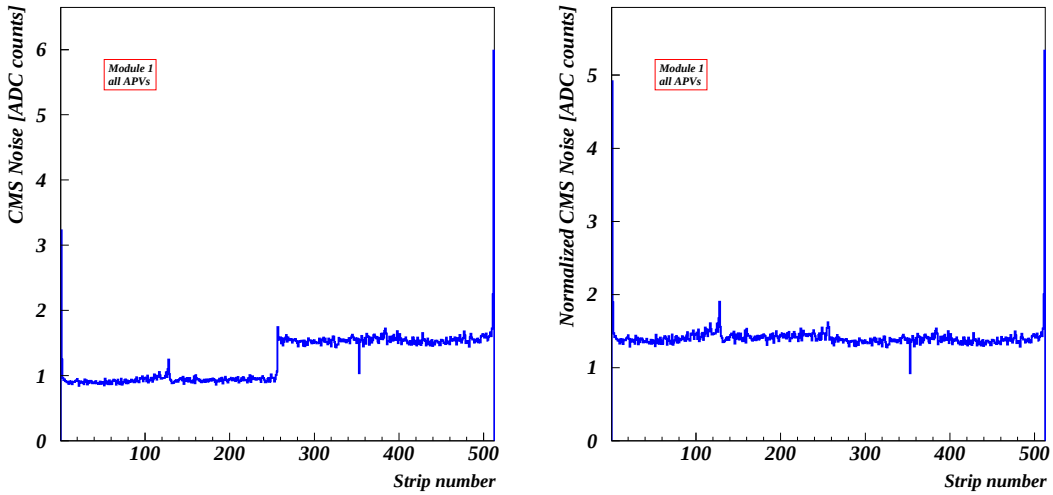

Figure 9: Profile of the common mode subtracted noise for a module before (left) and after (right) AOH gain normalization.

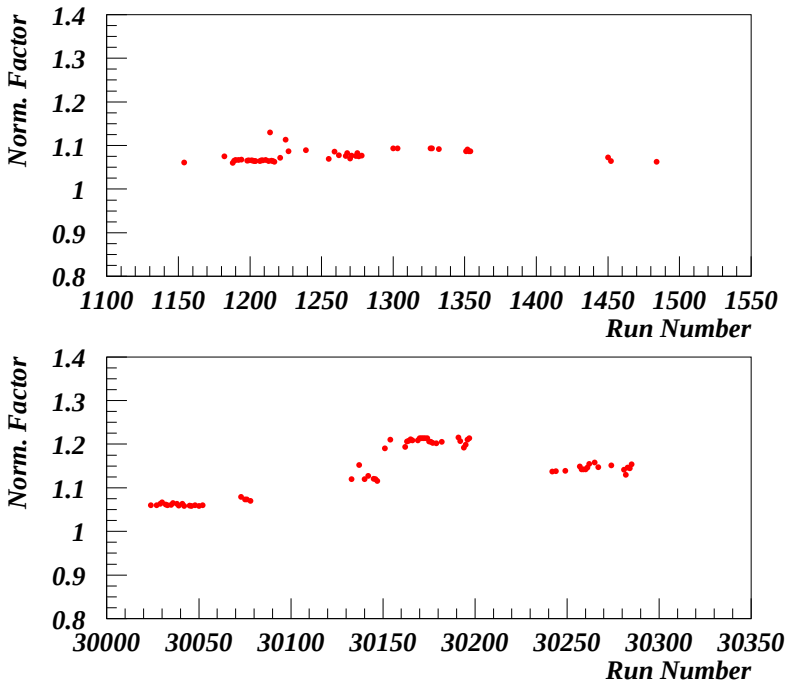

Figure 10: Time evolution of the normalization factor for the second AOH of one TIB module (top: TIB-only runs, $\sim$ 6 days of data taking; bottom: TIB-TOB joint runs $\sim$ 7 days of data taking). During the second phase of data taking the analogue optical fibres were disconnected and reconnected several times.

7 Beam Test Results

In this note the TIB modules under test (Tab. 2) are conventionally called TIB1, TIB2, TIB3 (upper string) and TIB4, TIB5, TIB6 (lower string), TIB1 and respectively TIB4 being the modules closest to the external cooling pipes visible on the left in Fig. 4. The TIB structure was placed with the module strips running horizontally.
Except for the last data taking period, when the structure was moved horizontally to test all six modules, the beam illuminated mainly the central module of both strings (TIB2 and TIB5). All other modules were powered, clocked and read out, but the number of clusters on those sensors was very low (i.e., mainly generated by noise or by highly scattered beam particles).

7.1 Beam profile

Figure 11 shows the vertical profile of the muon and pion beams as measured in the TIB2 and TIB5 modules.

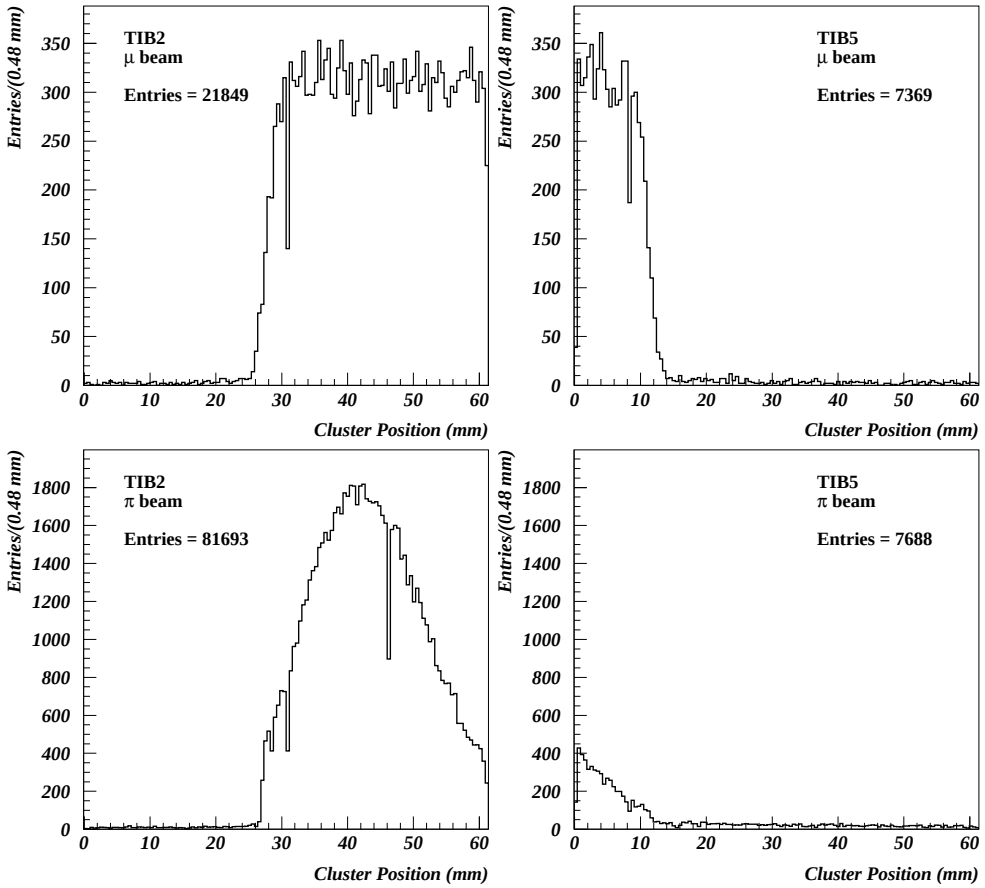

Figure 11: Muon (top) and pion (bottom) vertical beam profiles reconstructed in the TIB2 (left) and TIB5 (right) modules. The dips are due to noisy and less efficient strips.

Figure 11 also shows that the pion beam was much more tightly collimated (2 cm FWHM) than the muon beam (the 4.5 cm trigger scintillator "shadow" is clearly visible in the upper plots of Fig. 11, the real muon beam dimensions being much larger). In fact, the X5 muon beam is obtained by in-flight pion decays during the ~ 300 m path from the production target to the final absorber, which is placed some metres before the detector station to stop the residual pion components when the muon beam is selected. In this way the muon transverse momentum (with respect to the beam line) keeps memory of the neutrinos emitted in the pion decay during the very long flight from the production target to the detector, which results in the increase in the beam spot area. The muon beam intensity was also much lower than what could be obtained with pions.

7.2 Bias voltage scans

In this section data coming from microstrip module bias voltage scans are reported. The scans were performed up to a maximum value of 500 V in 50 V steps. The peculiar behaviour observed when reverse (ramp-down) scans took place with short waiting time between steps and under high relative humidity conditions is described in Sect. 7.4.

7.2.1 Current vs. bias voltage

The power supply high voltage (HV) lines are organized in such a way that the three detectors of each string are connected to a single HV channel. Figure 12 shows the reverse current of the two strings as a function of the bias voltage. The measurements were performed at room temperature (about 25 °C, see Fig. 5 where the dry gas temperature inside the TIB box is shown) with the module front-end electronics powered and clocked. The current

of each string of modules, measured at a bias voltage of 400 V, was about 800 nA.

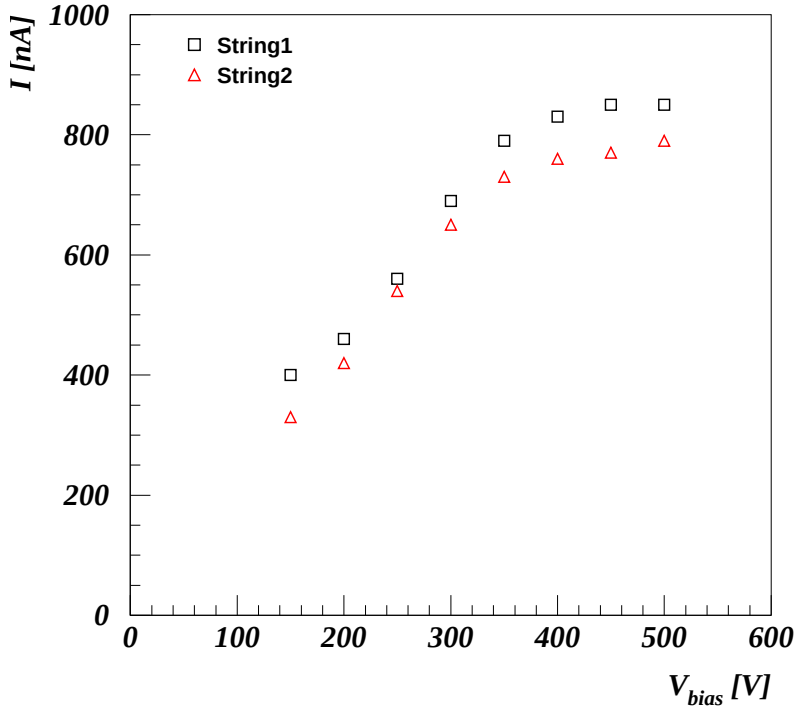

Figure 12: Reverse current as a function of the bias voltage for the two TIB strings.

7.2.2 Signal-to-noise ratio vs. bias voltage

One of the most important parameters characterizing a silicon microstrip detector is the signal-to-noise ratio. This parameter is related both to the charge collection efficiency and to the strip noise which in turn depends on the electronics, sensor capacitance and bias current. Most of these factors (collected charge, sensor capacitance and bias current) depend on the bias voltage: strongly when the silicon bulk is still not completely depleted, mildly once the depletion voltage has been reached.
Figure 13 shows the average strip noise (left) and the signal-to-noise ratio (right) for the central module of each string as a function of the bias voltage. As expected, the noise curves taken with the two different modules

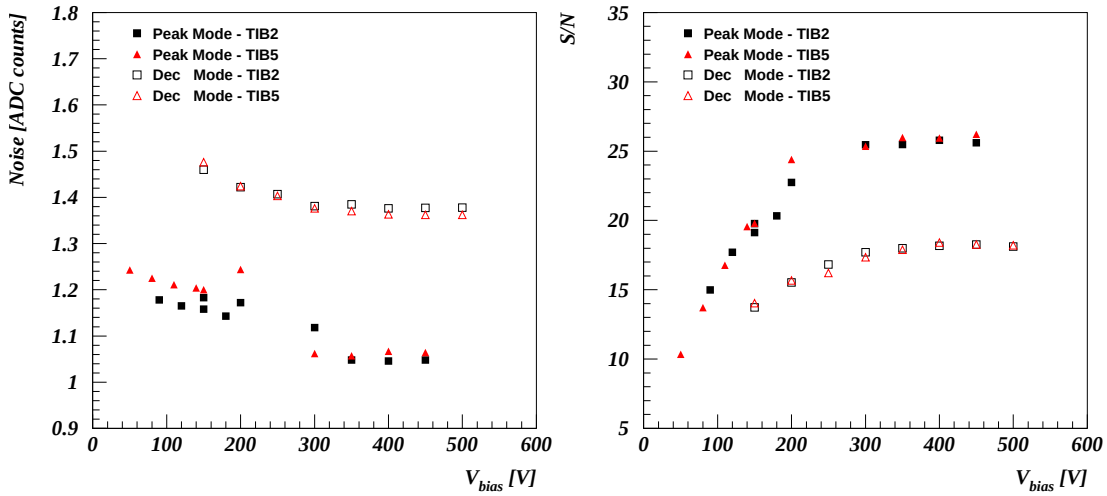

Figure 13: Strip noise (left) and signal-to-noise ratio (right) for TIB2 (squares) and TIB5 (triangles) as a function of the bias voltage. Data in peak (full symbols) and deconvolution (open symbols) mode are shown. Scattered points around 200 V in peak mode come from the “ramp-down” scans discussed in 7.4.

operating in the same mode almost overlap. The average common mode subtracted module noise decreases with increasing bias voltage, until it reaches the asymptotic values of 1.06 ADC counts in peak mode and 1.38 ADC counts in deconvolution mode.
Figure 13 (right) shows the signal-to-noise ratio for the two modules, in both APV25 operating modes, as a function of the bias voltage. The increase of the S/N ratio as a function of the bias voltage results from the greater collected charge with the increase in the depleted region, but also, after the sensor has reached complete depletion, on a small observed increase of the APV25 response to faster charge collection at its input (ballistic effect) and to a reduction in the residual noise. The nominal sensor depletion voltage for the TIB2 and TIB5 modules, as measured using the sensor C-V characteristics (Tab. 2), is 183.4 V and 137.9 V respectively. Figure 13 (right) shows that, from the signal-to-noise ratio point of view, the depletion voltage derived from the C-V curves is not the optimal detector working point. In fact, at this voltage the S/N ratio is approximately $\sim$ 80% of the asymptotic value. This means that the silicon microstrip modules must be operated in "over-depletion" mode when the S/N issue becomes critical (i.e., when the tracker will be heavily irradiated and the S/N value will be considerably reduced with respect to the initial phase of the experiment).
The S/N asymptotic value measured in deconvolution mode is lower than the peak mode one by approximately 30%. In fact, as explained in [13], the deconvolution filter effectively decreases the signal duration to match the LHC bunch crossing frequency, but at the expense of an increase of the noise level.
The signal-to-noise ratio values reached by the TIB detectors when they are overdepleted are shown in Table 4. In the same table the expected values are also shown. Fluctuations of $\pm$0.5 units on the S/N ratio, depending on the run, have been observed. Uncertainties on the expected values (coming from APV25 noise characteristics, sensor capacitance and active depth) are $\pm$0.5-1 units.

Table 4: Measured and expected signal-to-noise ratios in peak and deconvolution mode, in overdepletion regime.

	Signal-to-noise ratio		
Readout mode	TIB2	TIB5	Expected
Peak	25.5	26.1	27.1
Deconvolution	18.1	17.8	17.5

The expected signal-to-noise ratios are calculated using the following procedure: for the signal, one must take into account the energy loss in silicon [33] by 120 GeV/c muons, the sensor active depth (290 μm) and the energy needed to produce an electron-hole pair in silicon (3.62 eV/pair). This results in a most probable value for the signal of about 23600 e^- for a normally impinging 120 GeV/c muon [9)]. For the noise calculation, the sensor capacitances and resistances ($C_{interstrip}$, C_{bulk}, $C_{PitchAdapter}$, R_{Strip} and R_{bias}), the bias current and the AOH noise figure are used. For a TIB IB2 type sensor the total capacitance, as measured in the Process Quality Control centre, is 14.2 pF [34]; the AOH Equivalent Noise Charge (ENC) has been estimated to be 190 electrons [35], R_{bias} is 1.5 MΩ, while R_{Strip} is 77 Ω. The bias current contribution is negligible for a non-irradiated module.
The best noise estimate (ENC) for an IB2 type module, using the APV25 noise parametrization [11], is 870 and 1350 electrons in peak and deconvolution mode respectively.

7.2.3 Cluster width vs. bias voltage

Figure 14 shows the mean cluster width as a function of the bias voltage for the TIB2 and TIB5 modules when operated in deconvolution mode. The cluster width continues to decrease even after the nominal depletion voltage is reached because of lower charge-sharing between strips, which is in turn driven by a decreasing strip capacitive coupling.
The mean cluster width reaches the asymptotic value of 1.5 and 1.7 for the TIB2 and TIB5 modules, respectively. This difference is explained by geometrical considerations: in the structure used for this test the modules of two adjacent strings form an angle of 7.8°. Due to this arrangement, the particles enter the TIB2 module orthogonally, while the TIB5 module is slightly tilted with respect to the beam direction and the charge produced by particles crossing the silicon microstrip module is distributed underneath a larger path ($\sim$ 1/3 of the strip pitch). The ratio of the two widths (also shown in Fig. 14) is independent from the bias voltage when the sensor is over-depleted. A similar behaviour has been found in peak mode.

[9)] The expected signal in the slightly tilted (7.8 deg.) TIB5 module is higher by $\sim$1% with respect to the vertically placed TIB2 module. This small contribution has been neglected in Table 4.

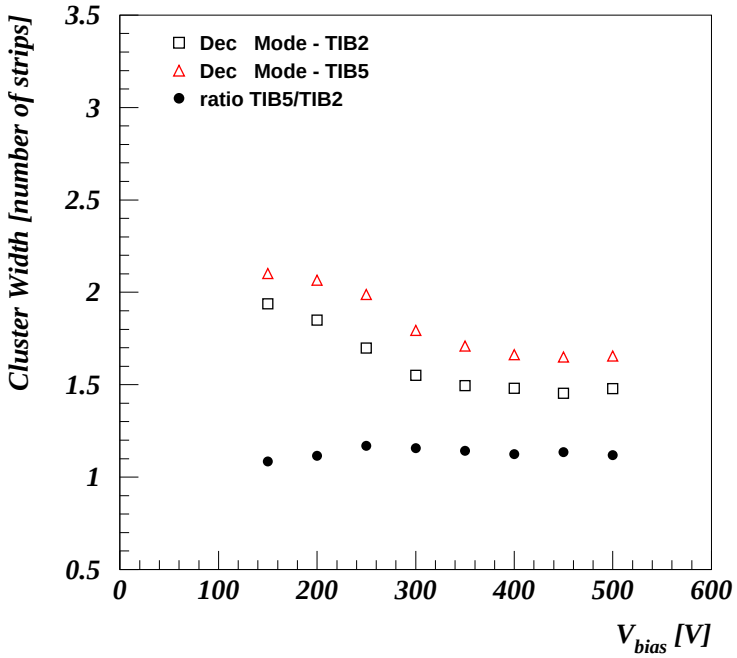

Figure 14: Mean cluster width as a function of the bias voltage for the TIB2 (triangles) and TIB5 (squares) modules operated in deconvolution mode. The ratio of the two widths is reported also (full circles).

7.3 Detector overlap

In order to guarantee spatial hermeticity for particles coming from the interaction region of the CMS detector and to ease the alignment procedures for the final tracker, the sensitive areas of two adjacent strings have a small overlap region. This area extends approximately 1.5 mm ($\sim$ 12 strips) in the direction orthogonal to the strips. With such an overlap, a small fraction of particles crosses both the TIB2 and the TIB5 modules and their hits are obviously correlated position-wise. Figure 15 shows this correlation in the overlap region, demonstrating the possibility to have double hits in the same layer of the tracker.

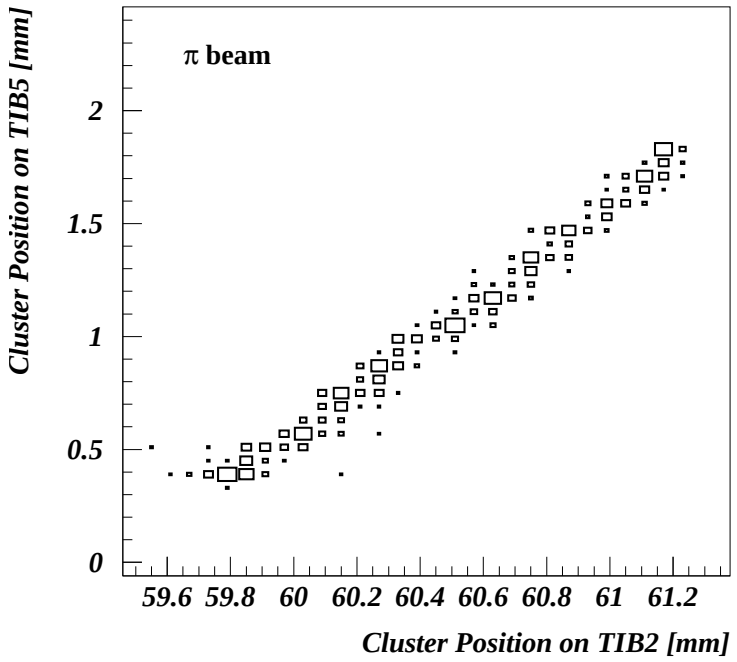

Figure 15: Hit position in TIB2 vs. hit position in TIB5 for the overlap region.

7.4 Hysteresis effects

During the beam test some of the voltage scans were performed with a full cycle of the bias voltage from zero to a maximum value well above depletion and back to zero. During the "ramp-up" phase the signal and noise performance are those expected from previous measurements, whereas in the "ramp-down" phase a clear reduction of the signal-to-noise ratio was observed ("hysteresis effect"). Figure 16 shows the S/N ratio measured in deconvolution mode as a function of the bias voltage during a bias cycle. A very similar behaviour has been observed in peak mode.

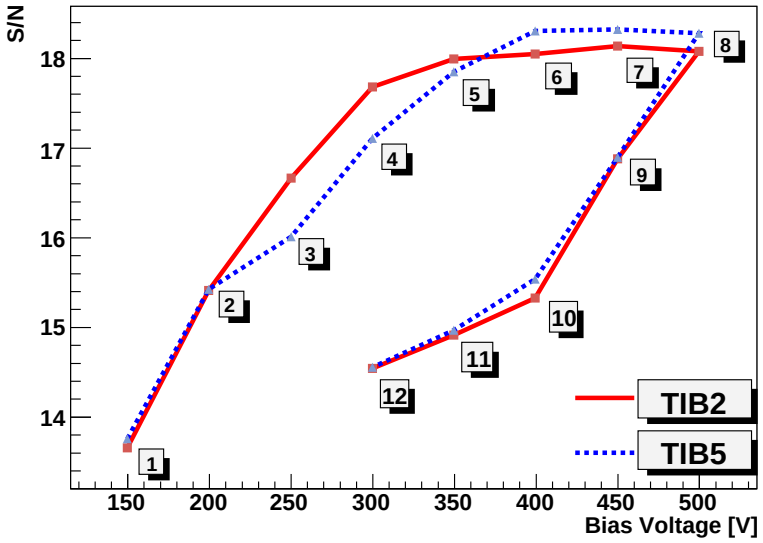

Figure 16: S/N ratio for modules TIB2 and TIB5 as a function of the bias voltage during the voltage scan cycle in deconvolution mode. The numbers next to each data point indicate the time ordering of the measurements.

The maximum size of the effect on the S/N ratio is around 17% in both APV25 operating modes and it can be decomposed in an 8% decrease of the signal and a 9% increase of the noise (Fig. 17).

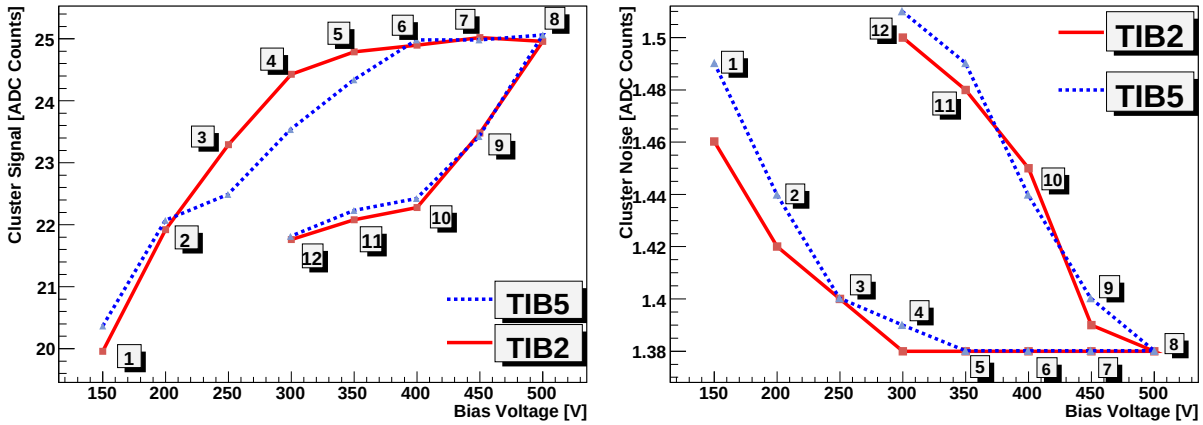

Figure 17: Signal (left) and noise (right) performance of modules TIB2 and TIB5 as a function of the bias voltage during the voltage scan cycle in deconvolution mode. The numbers next to each data point indicate the time ordering of the measurements.

The hysteresis effect is also observed in the average cluster width, which increases by about 16% in the ramp-down runs. The systematic difference on the cluster width among the two modules reflects the fact that module TIB2 is perpendicular whereas module TIB5 is inclined with respect to the beam direction (Fig. 18).

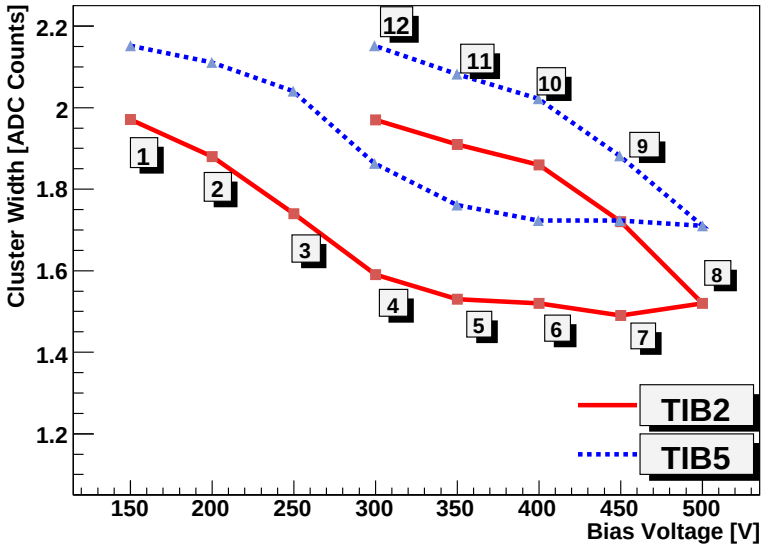

Figure 18: Average cluster width for modules TIB2 and TIB5 as a function of the bias voltage during the voltage scan cycle in deconvolution mode. The numbers next to each data point indicate the time ordering of the measurements.

7.4.1 Laboratory measurements on TIB test-structures

The set of measurements on the module performance described in the previous paragraph can be partially explained by an increase in the inter-strip capacitance (C_{int}) of the sensors during the bias voltage ramp-down.
A dedicated study has been carried out in the laboratory to test this assumption using test-structures extracted from the wafers of the TIB sensors and used in the Process Quality Control (PQC) of the silicon strip tracker detectors [6]. The IS-CAP-AC structures, used in the PQC to monitor the interstrip capacitance of the sensors, have undergone voltage cycles similar to those applied to the modules during the beam test and these operations have resulted in an increase of C_{int} while bringing the bias voltage back to zero (Fig. 19).

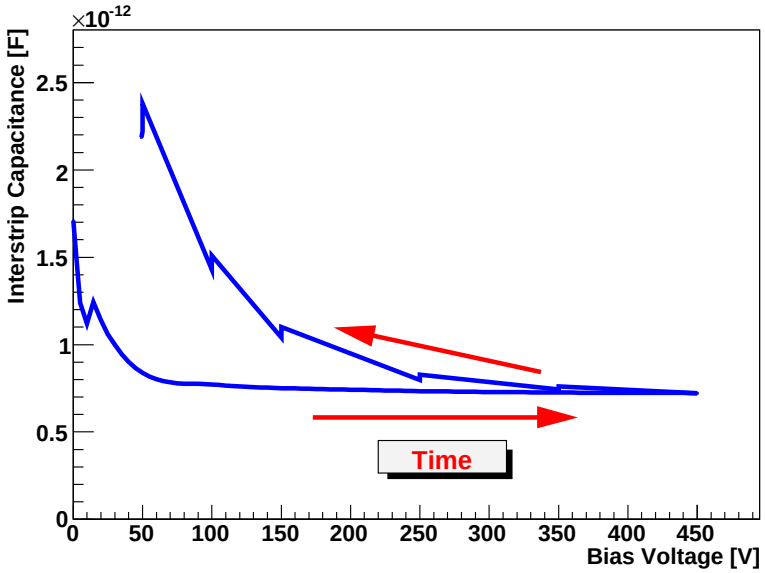

Figure 19: Interstrip capacitance measured with an IS-CAP-AC test-structure of a TIB wafer during a voltage scan cycle. The arrows indicate the time ordering of the measurements. The sharp edges in the plot are due to multiple measurements performed after the bias value had been kept constant for several minutes. This behaviour demonstrates that the hysteresis effect decreases with time.

During this study it was possible to correlate the onset of the hysteresis effect with the environmental conditions. The inter-strip capacitance depends on the bias voltage history of the structure only when the measurements are performed in high relative humidity (RH), above 30-35%, as it was the case for the cycle shown in Fig. 19. At lower values of relative humidity no hysteresis effect was observed.
An explanation of the phenomenon could be the different arrangement of the mobile charges at the Si-SiO_2 interface in the presence of high RH. This effect depends on the fabrication details of the oxide layer and it is not observed for the TOB modules installed in this beam test, which were built with sensors from a different producer [36].
The beam test voltage scans shown in Figs. 16, 17 and 18 were performed at values of RH around 45-50% (first part of Fig. 6). An additional voltage scan with varying RH levels confirms the hypothesis, since after dry air was used to flush the system (second part of Fig. 6) the hysteresis effect ceased (Table 5). This is demonstrated by comparing the S/N pair values taken at equal voltage reached during ramp-up and ramp-down scans (e.g., runs # 30147-30169, 30163-30166, 30142-30170 on Table 5).

Table 5: S/N ratio for the TIB2 module as function of the bias voltage during a voltage scan cycle in deconvolution mode performed at RH around 3%. The entries (run number) are in the same order in which the runs were taken.

Run no.	Bias Voltage [V]	S/N
30142	200	16.9
30145	250	17.2
30147	300	17.5
30162	350	18.4
30163	400	18.5
30164	450	18.5
30165	500	18.5
30166	400	18.4
30169	300	18.1
30170	200	17.1
30172	450	18.4
30173	300	18.0
30174	350	18.2
30175	350	18.5

7.5 TIB silicon microstrip module uniformity response

7.5.1 TIB uniformity orthogonally to the strips

In order to analyse the uniformity of the detector, the behaviour of the main variables related to the silicon microstrip module performance was studied as a function of the cluster position in the direction perpendicular to the strips.
A large number of events was collected under stable running conditions to ensure a large number of clusters on all strips. The high intensity 120 GeV/c pion beam was used in order to reduce the duration of the data taking period. The beam centre was placed in the central module of the upper string, so that a large amount of data was collected in correspondence of the third and fourth front-end chips of TIB2 and on the first chip of TIB5. The total number of collected clusters was $\sim 1.5 \times 10^6$, with a number of clusters associated with each strip which varies in the range $1 \div 8 \times 10^3$. Data were taken in peak mode with the sensors biased at 350 V.
A cluster was associated with a strip if the reconstructed position x lay within a region one half-pitch on either side of the strip center. For each measured variable in a certain region, the uniformity parameter was defined as the ratio between the RMS and the mean value of the corresponding distribution in this area. Small regions around noisy strips, usually the first and last APV25 channels, were ignored.
The cluster noise distribution as a function of the APV25 channel is shown in Fig. 20 (left) for one of the APV of module TIB2. An example of a gaussian fit used to extract the cluster noise associated with a given strip is shown in Fig. 20 (right). The global cluster noise uniformity is of the order of 1.3% (1.7% for TIB2 chip 3, 1.5% for TIB2 chip 4 and 0.8% for TIB5 chip 1).
The cluster charge distribution as a function of the associated APV25 channel is shown in Fig. 21 (left) for the same

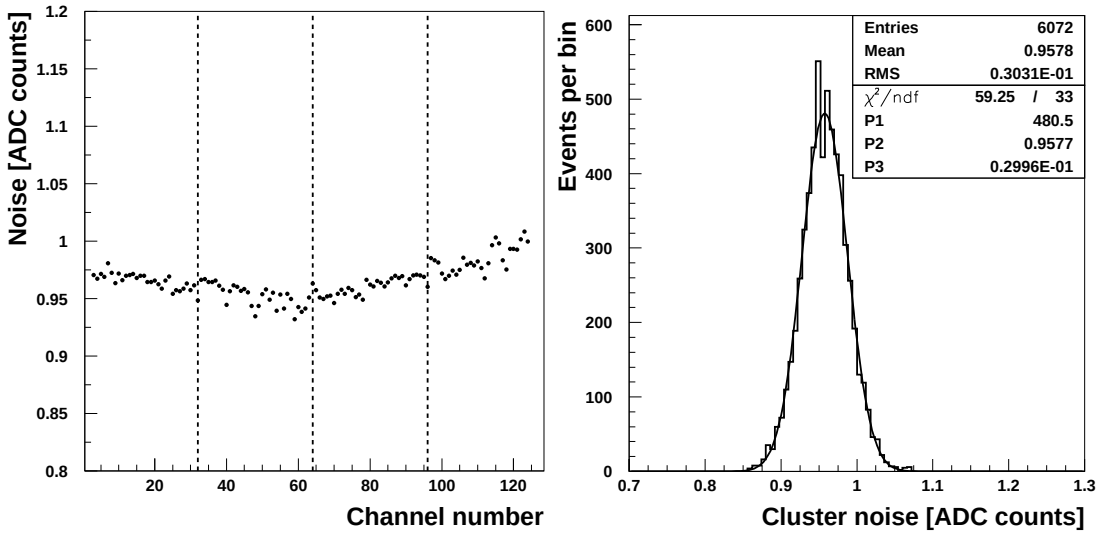

Figure 20: Cluster noise as a function of the strip number for the fourth APV25 chip of TIB2 (left) and example of cluster noise distribution and fit for one strip (right). Vertical lines separate 32-strip regions.

APV25 chip of Fig. 20. An example of a fit with a Landau-like function to extract the most probable value of the cluster charge associated with a given strip is shown in Fig. 21 (right). In some cases, in the charge distributions, a structure (modulo 32 strips) is visible. This could be due to the common mode calculation algorithm or to the tree structure of the APV25 analogue multiplexer[10)] which both involve a 32-channels grouping.

In Fig. 21 (left) the last group has a charge that is on average greater than the other three by approximately 0.5 ADC counts (i.e., $\sim 2\%$). The global charge uniformity is of the order of 1.4% while it is 1.9% for TIB2 chip 3, 1.0% for TIB2 chip 4 and 1.0% for TIB5 chip 1. The charge uniformity calculated over groups of 32 strips is of the order of 0.5%.

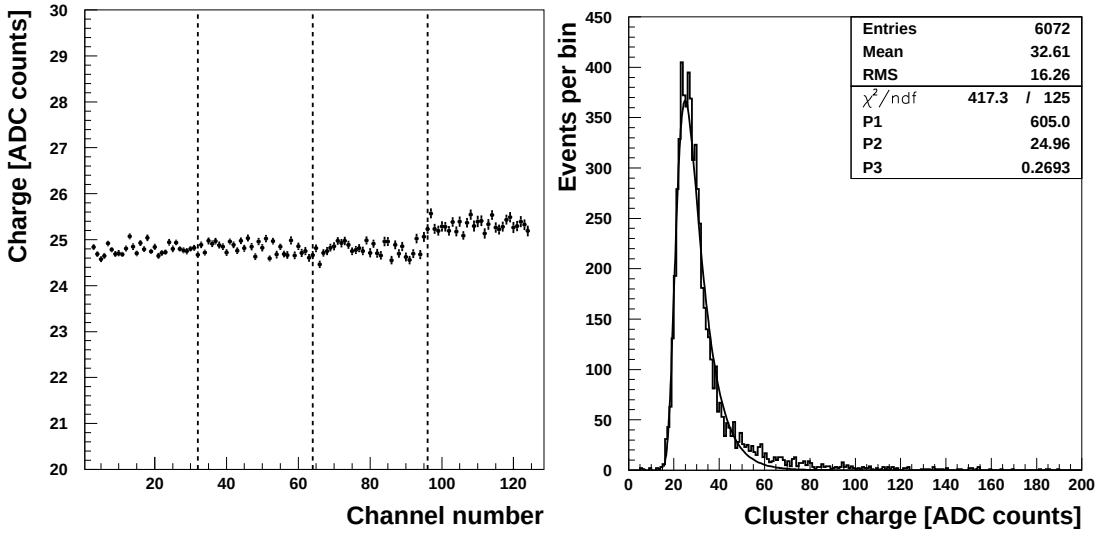

Figure 21: Cluster charge as a function of the strip number for the fourth APV25 chip of module TIB2 (left) and example of cluster charge distribution and Landau fit for one strip (right). Vertical lines separate 32-strip regions.

The signal-to-noise ratio distribution as a function of the channel for the fourth APV25 of TIB2 is shown in Fig. 22. The S/N ratio is smaller next to the edge of the chips due to an higher noise in these regions. The global RMS/mean ratio is around 1.6% (1.8%, 1.5% and 1.7% for TIB2 chips 3 and 4 and TIB5 chip 1, respectively) and around 1.0%

[10)] The order in which the APV25 channels are read out through the analogue output is non-consecutive: the physical channel number n_{APV25} as a function of the n^{th} channel appearing on the multiplexer output is given by the formula: $n_{APV25} = 32 * (nMOD4) + 8 * INT(n/4) - 31 * INT(n/16)$.

if calculated over groups of 32 strips.

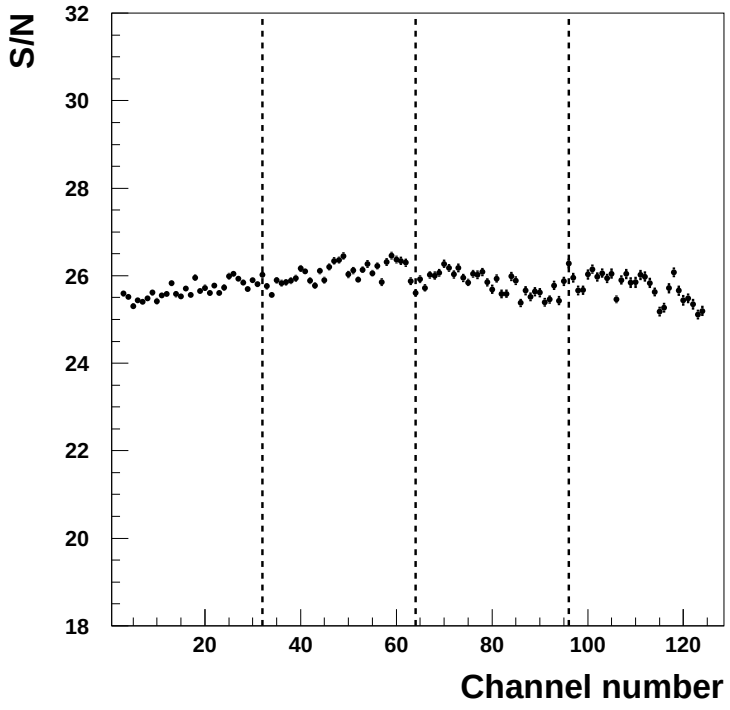

Figure 22: Cluster signal-to-noise ratio as a function of the strip number for the fourth APV25 chip of TIB2. Vertical lines separate 32-strip regions.

7.5.2 TIB uniformity along the strips

The TIB module performance was also investigated as a function of the cluster position along the strip. The 120 GeV/c muon beam was used in this study since it has an uniform particle density and covers the full area of the trigger scintillators. Three different runs were taken with the mechanical structure in different positions in the horizontal direction to investigate the full length of the central TIB modules. A total of 36000 events were collected for each APV25 chip. In these runs, modules were operated with a bias voltage of 400 V and operated in deconvolution mode.

The TIB cluster position along the strip was obtained from TOB detectors, since their strips were perpendicular to TIB ones. A linear transformation was used to obtain the TIB cluster position along the strip from the cluster position in TOB module. The transformation is of the type: $y_{TIB} = p_{TOB} \times n_{TOB} + c_i$, where y_{TIB} is the TIB cluster position along the strip, n_{TOB} is the TOB cluster strip position, p_{TOB} is the TOB sensor pitch (i.e., 183 μm) and c_i is a constant coefficient for the i^{th} TIB structure position. The c_i parameter is obtained, for each position of the TIB structure, using the "shadow" of the TIB detectors on the TOB (i.e., the falling edge of the hit position distribution in the TOB detectors, ${n_{TOB}}^{shadow-i}$, when a hit is present in the TIB too, Fig. 23). In fact $y_{TIB} = 0$ when $n_{TOB} = {n_{TOB}}^{shadow-i}$, so $c_i = -p_{TOB} \times {n_{TOB}}^{shadow-i}$. The accuracy on the TIB cluster position along the strip is dominated by the width of the edge region, mainly due to the beam divergence projected over the distance between TIB and TOB detector planes. Another source of error could come from the fact the neither TIB nor TOB detector modules are perfectly aligned (only linear displacements are considered). This accuracy has been estimated to be of the order of 2.5 mm.

TIB module clusters were grouped according to their position along the strip in 24 intervals (each one corresponding to 5 mm). The main variables related to detector performance were then plotted, with about 1500 events per interval.

The charge distribution as a function of the position along the strip is shown in Fig. 24 (left) for one of the APVs chips analysed. The charge uniformity of this distribution is 1.4%. The signal-to-noise ratio distribution as a function of the position along the strip is shown in Fig. 24 (right) for the same APV25 chip. The S/N uniformity along the strip is again 1.4%.

Sometimes the numbers shown in the last two sections exceed the pure statistical fluctuations and systematics should be taken into account to fully explain them. Certainly the common mode subtraction scheme, which uses a

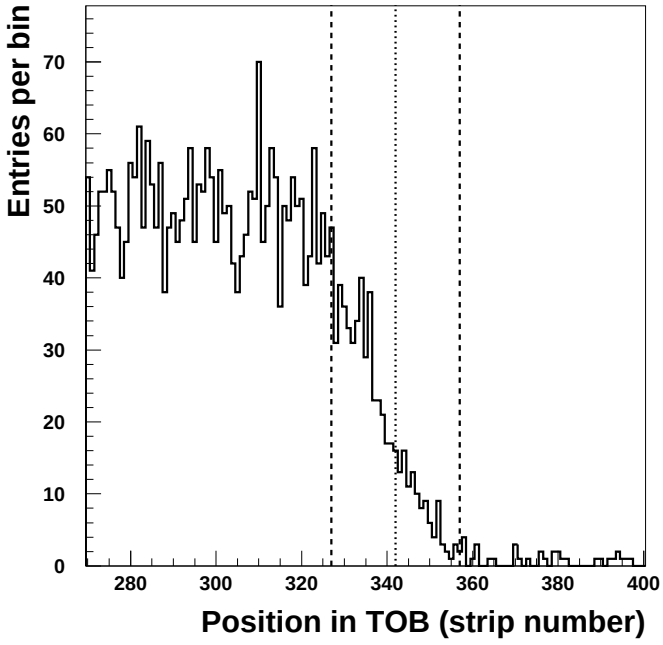

Figure 23: Cluster position in the first TOB module when a hit is present in the central TIB module. The vertical lines indicate the edge region used to calculate the TIB hit coordinate along the strip.

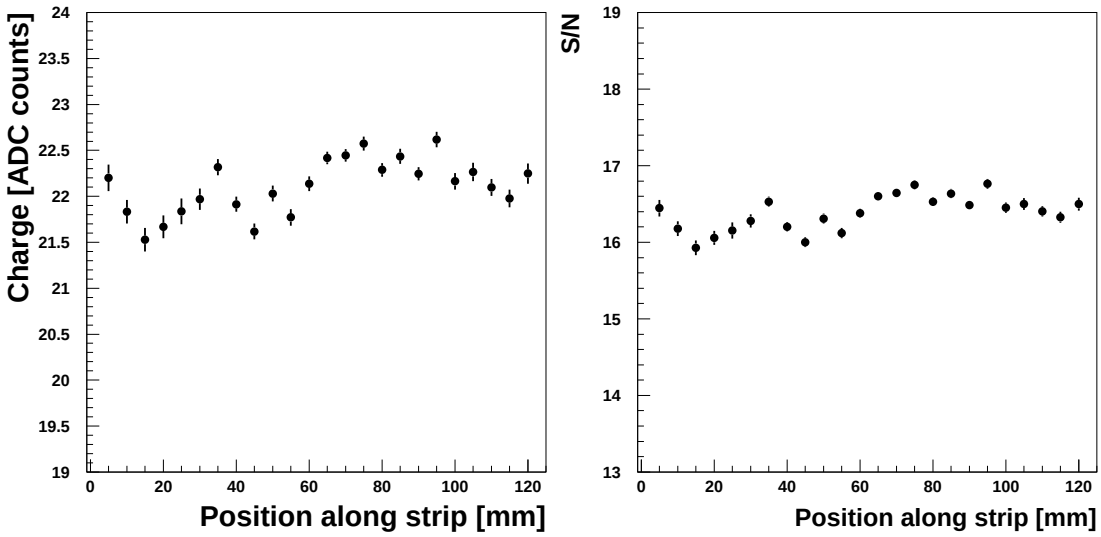

Figure 24: Cluster charge (left) and signal-to-noise ratio (right) as a function of the position along the strip (starting from the hybrid side). Error bars indicate the statistical error on the fit only. Detectors are operated in deconvolution mode.

32-strip grouping, is one of the sources of systematic effects. Other possible sources can be found in APV25, sensor and optical chain non-uniformities, but these are difficult to quantify. In any case, the level of non-uniformity shown in this section is of the order of 1-2%. These numbers can be taken as a possible reference figure when quoting the overall errors on cluster-related quantities.

7.6 Time evolution of the signal

The purpose of this study is to investigate the time evolution of a particle signal as seen by the APV25 on a TIB module. The knowledge of this behaviour will be useful to fine-tune the detector front-end electronics, especially when the LHC will reach the high luminosity regime. As can be seen in this section, the signal amplitude, the fake cluster rate, the eta functions and the cluster width depend, especially when the APV operate in deconvolution mode, on the choice of the sampling time.

7.6.1 Signal shape

To reconstruct the signal time evolution a certain number of runs were taken varying the phase difference between the APV25 clock and the SPS 25 ns beam clock via the PLL chip[11]. Coarser variations of the clock delay (steps of 25 ns each) can be obtained by changing the APV25 latency by one or more units (i.e., the chip pipeline column which is read out).
Figure 25 (left) shows the time evolution of the signal by plotting the reconstructed charge as a function of the delay while Fig. 25 (right) shows the Landau most probable value for each vertical slice of Fig. 25 (left). These pictures were prepared using data collected with TIB2 biased at 300 V and operating in peak mode. The ADC counts for each APV25 have been normalized to the same reference value using the procedure described in Sect. 6.2.

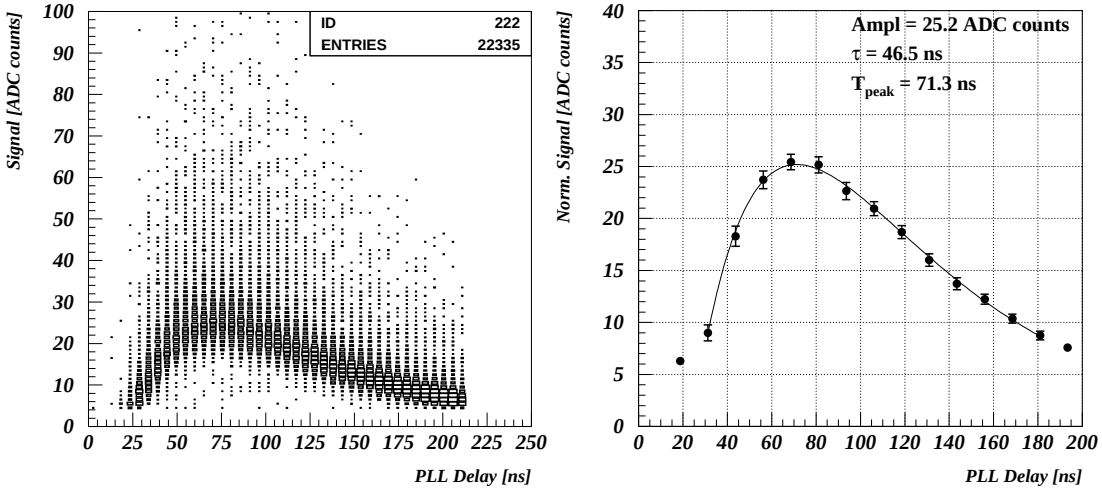

Figure 25: Cluster signal evolution as function of the PLL delay (left); reconstructed APV25 response curve (right). Data are taken with the TIB2 silicon microstrip module with the APV25 chips operating in peak mode and the sensor biased at 300 V.

Figure 25 (right) has been fitted with a CR-RC [12] shaper transfer function with a time constant τ. The best fit of the shaper time τ is, in this case, 46.5 ns, to be compared with an APV25 design value of 50 ns. The normalized signal peak amplitude is 25.2 ADC counts.
The value of the APV25 shaper time constant and the signal peak value can be trimmed by changing the parameters which control the shaper input FET current bias (called I_{sha}) and the shaper feedback voltage bias (called V_{FS}). To be more specific the former affects the signal rising time, while the latter regulates the signal falling time. Table 6 reports the results of the I_{sha} dependence of the shaper time constant and the signal amplitude while keeping V_{FS} fixed at a value of 60 (which corresponds to ~ 0.8 V). The same table also reports the signal maximum variation with respect to what is measured for an Isha register value of 40 (which corresponds to I_{sha}=40 μA).

Table 6: Shaper time constant (τ) and peak signal (S) variation as function of I_{sha} (V_{FS} being fixed to 0.8 V). APV25 are operated in peak mode.

$I_{sha}[\mu A]$	40	45	60	80
τ[ns]	48.7	46.5	46.1	43.4
Δ(S)	S=25.2 ADC counts	+4%	+6%	+12%

Table 6 essentially shows that by increasing I_{sha} the APV25 time response can be made faster and the signal higher. This increase, however, drives the APV25 outside the CR-RC shaper approximation introducing imperfections in the deconvolution filter, the weighting parameters of which were calculated for an ideal CR-RC shaper.

[11] The PLL can delay the clock in steps of 1.04 ns (i.e., 25 ns/24).

[12] A CR-RC shaper with time constant τ has a transfer function $h(t) = S_p \times \frac{t-t_0}{\tau} exp(-\frac{t-t_0}{\tau})$, where S_p is the signal peak amplitude and t_0 its starting time.

Figure 26 shows the APV25 time response function as measured in deconvolution mode with I_{sha} and V_{FS} values of 40 μA and 0.8 V, respectively.

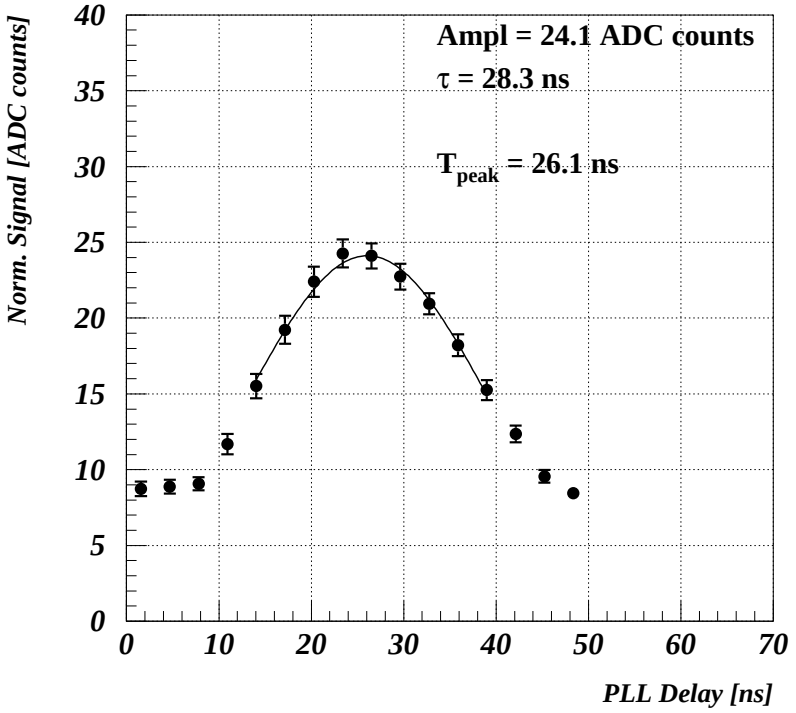

Figure 26: APV25 time response function in deconvolution mode, for the TIB2 silicon microstrip module biased at 300 V. A gaussian curve fitting the data is superimposed.

The rise-time of Figure 26 is conventionally defined as the time needed for the gaussian fitting the data points to pass from 10% to 90% of the maximum. In this gaussian approximation, the rise time is τ = 28.3 ns.
The APV25 shaper time constant and the signal dependence on the bias voltage are reported in Table 7 for APV operated in deconvolution mode. As can be seen, fuller sensor depletion increases the signal and slightly reduces the charge collection time.

Table 7: Shaper time constant (τ) and peak signal (S) variation as function of V_{bias} (V_{FS} being fixed to 0.8 V and I_{sha} to 40 μA). APV25 are operated in deconvolution mode.

V_{bias}[V]	250	300	350	400	450	500
τ[ns]	29	28.3	27.6	28.5	27.7	27.5
Δ(S)	S=23.3 ADC Counts	+3.2%	+5.7%	+5.7%	+6.6%	+5.3%

7.6.2 Cluster width

Figure 27 shows the mean cluster width as a function of the sampling time for data collected in peak (left) and deconvolution (right) modes. The two arrows indicate the maximum of the signal time response curves.
As can be seen in Fig. 27 the cluster width reaches the maximum much before the cluster charge does (25 ns in peak and 4 ns in deconvolution mode). To investigate this effect in detail, the signal time evolution for the cluster central and side strips has been studied separately (Sect. 7.6.3).

7.6.3 Charge on cluster side strips and eta function

For each cluster the seed strip and the two strips on either side, regardless of whether they belong to the cluster or not, have been selected. The seed strip signal is called S_{Seed}, while S_{High} and S_{Low} are the higher and lower signal

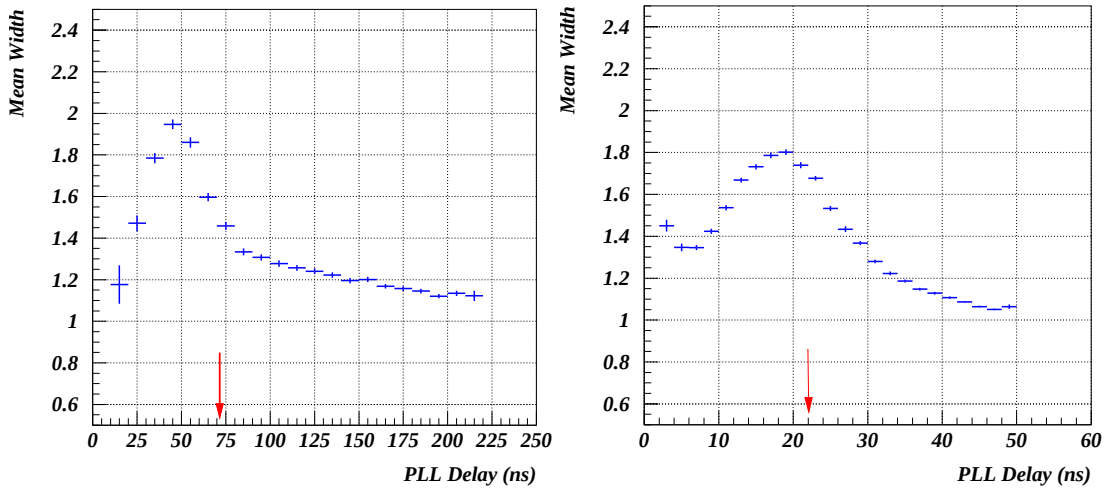

Figure 27: Mean cluster width as a function of the sampling time for data collected in the peak (left) and deconvolution (right) modes. The two arrows indicate the maximum of the signal time response curves.

on the two side strips. The events are divided into two categories depending on how the charge is shared among the strips. For this purpose the Eta function (η) has been used. It is defined in the following way: $\eta = S_R/(S_L + S_R)$ where S_R is the rightmost strip and S_L is the leftmost strip of the doublet of strips formed by the highest charge in the cluster and the higher of the two lateral strips (whether it belongs to the cluster or not).
Figure 28 shows the η distribution for the TIB2 silicon microstrip module operated in peak and deconvolution mode. The flat region with $0.2 \leq \eta \leq 0.8$ corresponds to events where the cluster charge is shared between two or more strips, while the two edge regions are mostly populated by single strip clusters. The gaussian dispersion of the two peaks is due to the fact that η is always calculated using two strips but in these regions only one actually collects particle generated charge, while the other mainly sees noise. Furthermore, when the "noise" strip measures a negative signal, the eta value can also be negative, or greater than one.
Figure 29 shows the signal time evolution for each strip in a cluster region when the η value is less than 0.2 or

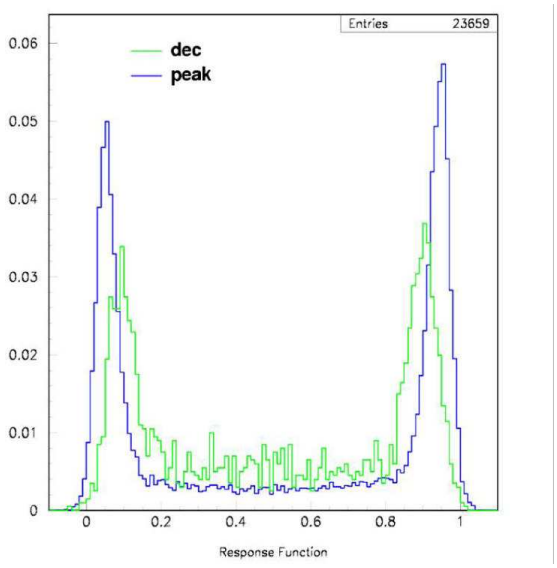

Figure 28: The η function for the TIB2 module operated in peak and deconvolution mode.

greater than 0.8 (mainly single strip clusters). Data were collected in peak (left) and deconvolution (right) mode. In this η region the cluster signal is mainly (95% of the total) due to the seed strip. The lateral strip signals peak faster than the seed strip signals (21.3 ns in peak mode and 6.2 ns in deconvolution mode) and they are generally not included in the cluster by the search algorithm due to their very low charge. For sampling times well after the peak, the lateral strip contribution becomes negative.

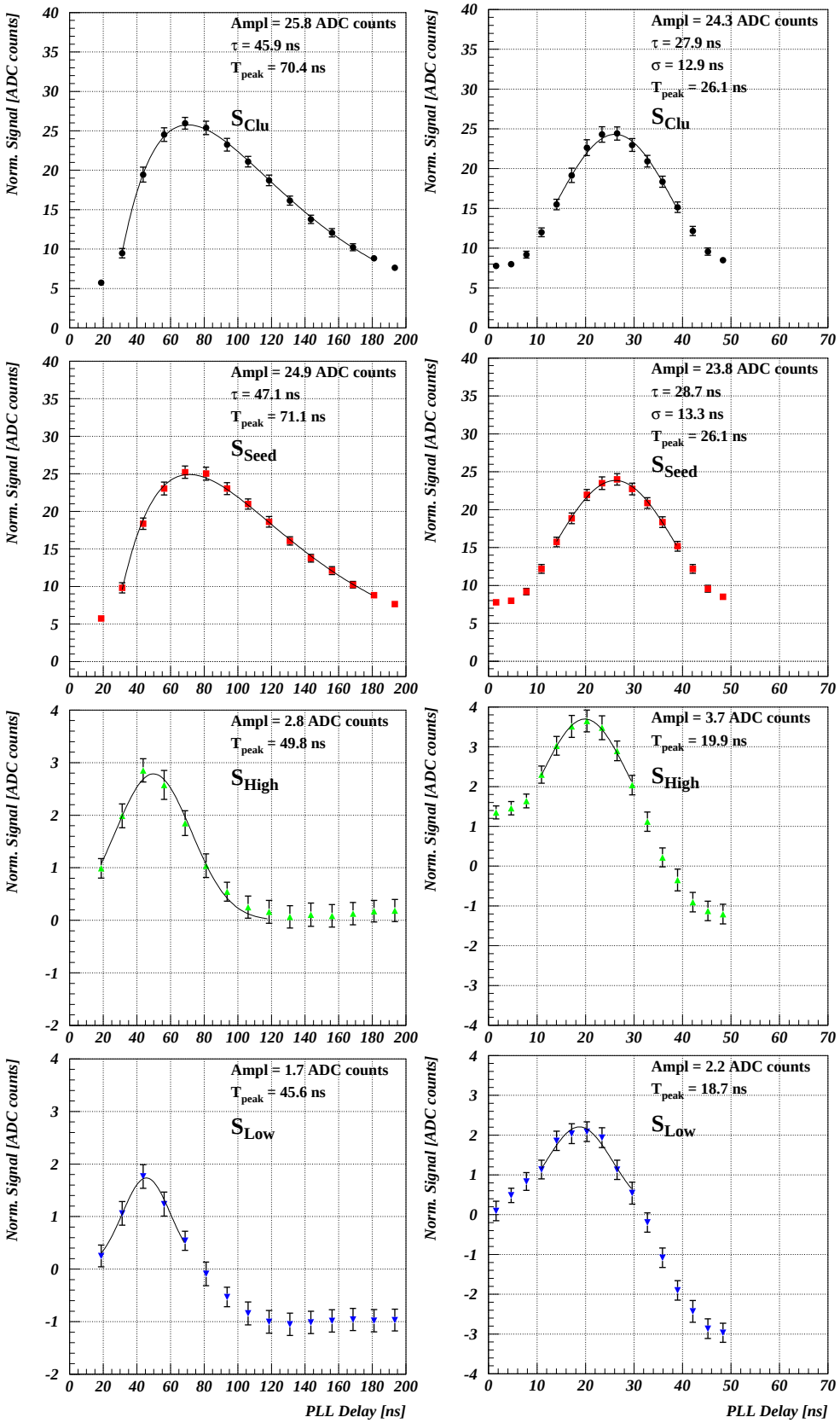

Figure 29: Signal time evolution for total charge (S_{Clu}), seed strip (S_{Seed}) and lateral strips (S_{High} and S_{Low}) for data collected in peak (left) and deconvolution (right) mode for clusters with η less than 0.2 or greater than 0.8 (single strip clusters).

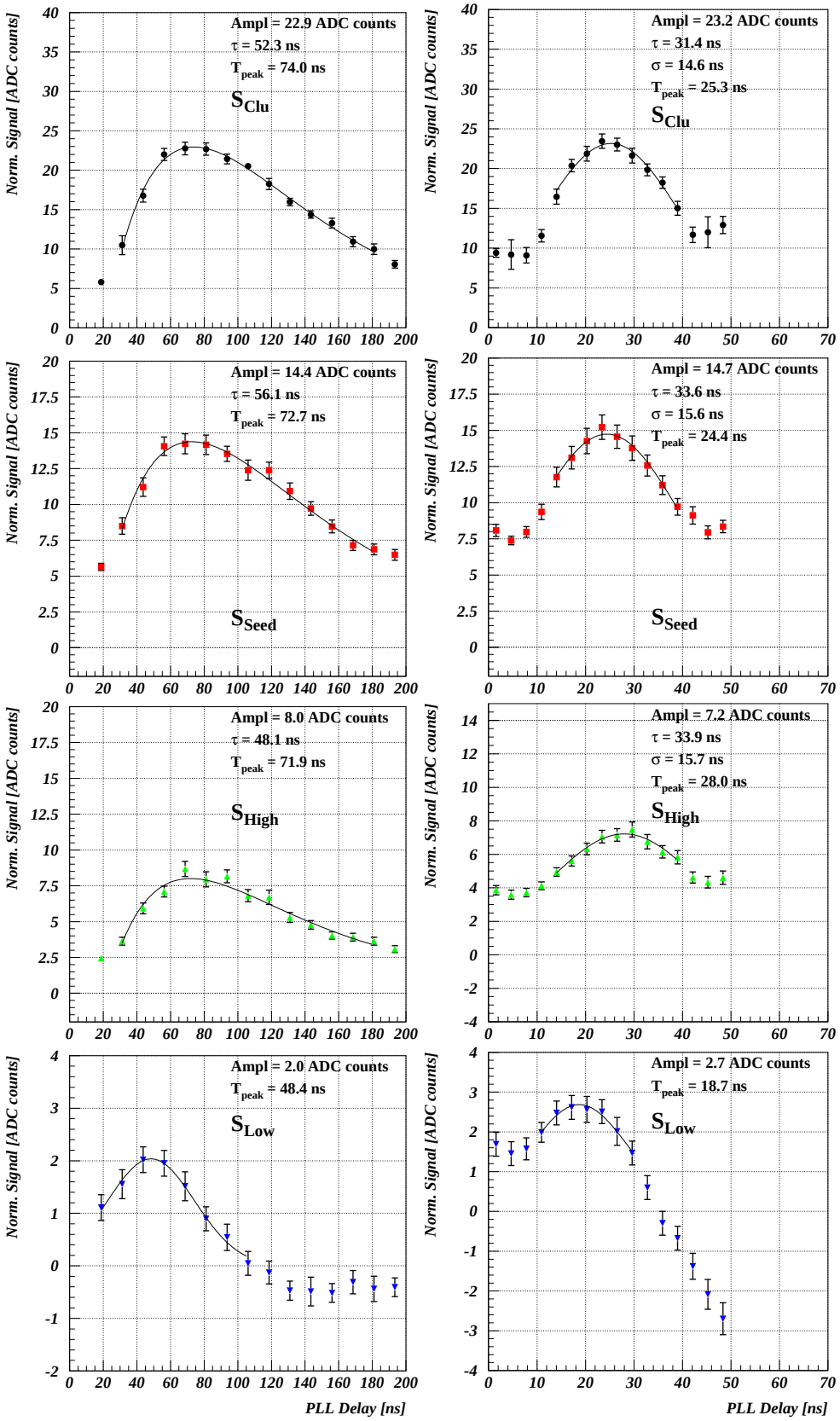

Figure 30: Signal time evolution for total charge (S_{Clu}), seed strip (S_{Seed}) and lateral strips (S_{High} and S_{Low}) for data collected in peak (left) and deconvolution (right) mode for clusters with η between 0.2 and 0.8 (multi-strip clusters).

In the region $0.2 < \eta < 0.8$ (Fig. 30) the lateral strip with a higher signal (S_{high}) is associated to the cluster by the search algorithm, and its time evolution is very similar to that of the cluster seed. The lower lateral strip signal continues to peak well in advance with respect to the cluster (26.1 ns in peak and 7.4 ns in deconvolution mode) and the undershoot is also present. Furthermore, when the cluster signal is spread on several strips the peaking and rising times are systematically longer than in the single strip cluster case.

Figure 31 shows the cluster signal evolution as a function of the PLL delay with respect to the trigger signal on a period greater than 50 ns. Data are taken in deconvolution mode using the 25 ns bunched pion beam.

The periodic structure reflects the fact that the beam has 25 ns bunched structure. In the case of a PLL delay

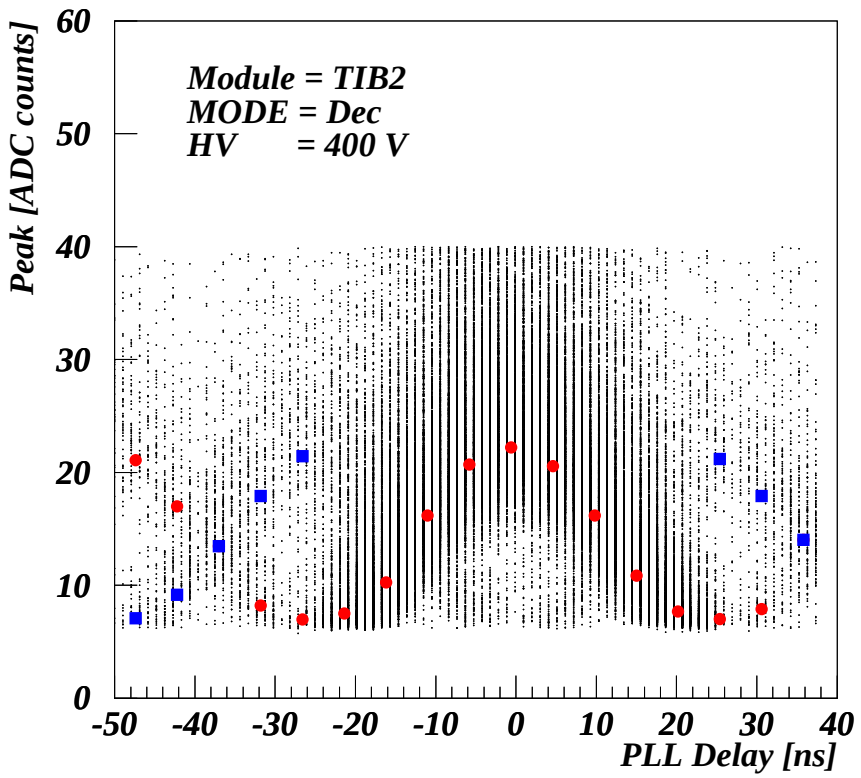

Figure 31: Cluster signal evolution as a function of the PLL delay. Data are taken in deconvolution mode. Round and squared symbols are used to guide the eye indicating the most probable charge values obtained with Landau fits of clusters grouped in 5 ns bins coming from in-time (round) and out-of-time bunches (squares).

multiple of 25 ns with respect to the optimal one (PLL delay = 0 ns), the APV25 detects signals coming from a (less populated) bunch which is not the one that has generated the trigger.

7.7 Power supply prototype comparison

The CAEN [37] power supply used during this beam test ran continuously for 18 days without any hardware reset or other problems. The LABEN [38] prototype has been used during the very last day: after the initial setup there were no hardware resets for the following data taking period. The interlock system never triggered while connected to the power supplies, but manual tests with artificial triggers to the interlock system were successful in correctly ramping down the high and low voltages before switching off the system.

The module performance, in terms of signal-to-noise ratio, when powered using the two power supply systems was identical (Fig. 32).

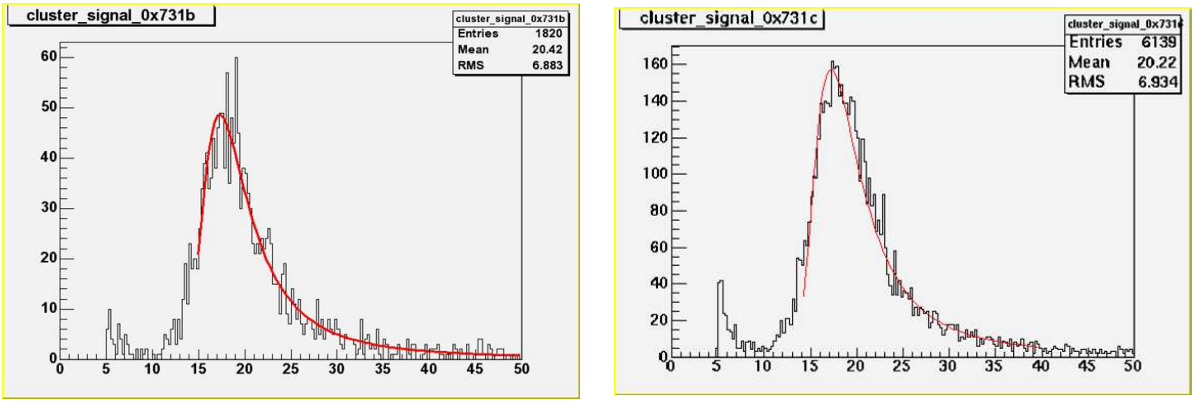

Figure 32: Signal-to-noise ratio measured in deconvolution mode with the CAEN (left) and LABEN (right) power supply prototypes (300 V bias voltage). The most probable value extracted from Landau fits is 17.6 in both cases.

8 Conclusions

A prototype of the third layer of the CMS TIB has been tested in a LHC-like 25 ns beam at CERN. The setup was assembled mostly using final tracker components, so this test can be interpreted as a system validation experiment. The performance of the detector was excellent, with a signal-to-noise ratio measured both in peak and deconvolution mode which is compatible with the expectations. Detector uniformity and signal time evolution have been studied, collecting information which will prove very useful for the understanding of the final detector behaviour. A peculiar hysteresis phenomenon, observed when the silicon microstrip sensors were operated during the ramping down phase of the bias voltage scan, was explained and traced back to an effect of the high relative humidity environment, which is unlikely to be reached during the real tracker operation.
Together with the important information gained on the silicon microstrip module behaviour, the test can also be considered a success from the system point of view. In fact the TIB setup was read out smoothly and the hardware and software commissioning took a very short time. The data acquisition system was able to read out TIB and TOB together with no problems. Specific commissioning procedures were implemented and studied in view of the by far more complex final tracker implementation.

Acknowledgements

The work described in this note would not have been possible without the efforts of all the people involved in the R & D and the construction of the CMS Inner Barrel Silicon Strip Tracker. We would like to thank the technicians who contributed to the beam test activities working at CERN or in the INFN laboratories. We would also like to express our gratitude to the CERN accelerator crew for the excellent performance of the special 25 ns beam.

References

[1] CMS Collaboration, *The Tracker Project Technical Design Report*, CERN/LHCC/98-6, April 1998; CMS Collaboration, *Addendum to the CMS Tracker TDR*, CERN/LHCC/2000-016, February 2000.

[2] Information about the dismissed X5 SPS experimental area can be found in: http://documents.cern.ch/archive/electronic/cern/preprints/sl/sl-2000-016.pdf

[3] D. Abbaneo, Nucl. Instr. and Methods A 518 (2004) 331, Erratum-ibid. A 525 (2004) 626.

[4] CMS Collaboration, *CMS Physics TDR*, Volume 1, CERN-LHCC-2006-001, 2 February 2006.

[5] L. Borrello, E. Focardi, A. Macchiolo and A. Messineo, Sensor Design for the CMS Silicon Strip Tracker, CMS NOTE-2003/020.

[6] J.L. Agram *et al.*, Nucl. Instr. and Methods A 517 (2004) 77.

[7] A. Honma, L. Feld, J. Labbe, M. Lenzi, M. Mannelli, A. Oh, P. Spagnolo and B. Surrow, An Automated Silicon Module Assembly System for the CMS Silicon Tracker, CMS NOTE-2002/005.

[8] P. Cariola *et al.*, Assembly of the Inner Tracker Silicon Microstrip Modules, CMS NOTE-2008/004.

[9] M. Axer *et al.*, Nucl. Instr. and Methods A 518 (2004) 321.

[10] S. Braibant *et al.*, Nucl. Instr. and Methods A 485 (2002) 343.

[11] M. French *et al.*, Nucl. Instr. and Methods A 466 (2001) 359.

[12] A. Marchioro, Deep submicron technologies for HEP, Proceedings of 4^{th} workshop on electronics for LHC experiments, CERN/LHCC/98-36,40.

[13] S. Gadomski, G. Hall, T. Høgh, P. Jalocha, E. Nygård and P. Weilhammer, Nucl. Instrum. and Methods A 320 (1992) 217.

[14] P. Murray, APVMUX User Guide,
http://www.te.rl.ac.uk/med/projects/High_Energy_Physics/CMS/APVMUXPLL/pdf/UserGuide.pdf

[15] M.Friedl, Nucl. Instr. and Methods A 518 (2004) 515.

[16] J. Troska, G. Cervelli, F. Faccio, K. Gill, R. Grabit, R. M. Jareno, A. M. Sandvik, F. Vasey, IEEE Trans. Nucl. Sci., Vol 50, No. 4, pp.1067. (2003).

[17] S.A. Baird *et al.*, The Front-End Driver card for the CMS Silicon Strip Tracker Readout, Eighth Workshop on Electronics for LHC Experiments, CERN/LHCC/2002-034.

[18] K. Kloukinas, A. Marchioro, P., Moreira and P. Placidi, A 40 MHz clock and trigger recovery circuit for the CMS tracker fabricated in a 0.25 μm CMOS technology and using a self calibration technique, LEB electronics workshop 1999, Snowmass (1999).

[19] I^2C Bus Specification, version 2.1, Philips Semiconductors (2000), document order number: 9398 393 40011.

[20] G. Magazzù, A. Marchioro and P. Moreira, IEEE Trans. Nucl.Sci. Vol. **51**, no. 4 (2004) 1333.

[21] C. Paillard, C. Ljustin, A. Marchioro, The CCU25: a Network Oriented Communication and Control Unit Integrated Circuit in a 0.25 μm CMOS Technology, Proceedings of the 8^{th} Workshop on Electronics for LHC experiments, CERN/LHCC/2002/034

[22] F. Faccio, P. Moreira, and A. Marchioro, Proc. SPIE, vol. 4134, 185, Oct. 2000.

[23] C. Ljuslin, C. Paillard, FEC Front End Control unit for Embedded Slow Control, Draft 0.84, 2003, CERN.
http://cmstrackercontrol.web.cern.ch/CMSTrackerControl/manuals.htm

[24] J. Coughlan et al., A PMC based ADC card for CMS Tracker readout, Proceedings of the 5^{th} Workshop on Electronics for LHC experiments (1999), CERN 99-09

[25] Hamamatsu Photonics K.K., Hamamatsu-City, Japan.

[26] Trigger Sequencer Card User Manual,
ftp://lyoftp.in2p3.fr/cms/Tsc/tsc03.pdf

[27] B.G. Taylor, Timing Distribution at the LHC, Proceedings of the 8^{th} Workshop on Electronics for LHC experiments, CERN/LHCC/2002/054
TTC website: http://ttc.web.cern.ch/TTC/intro.html

[28] L. Mirabito, Tracker Data Acquisition user guide, CERN 2003,
http://cmsdoc.cern.ch/cms/cmt/System_aspects/Daq/tkdaq.pdf
J. Gutleber *et al.*, Using XDAQ in Application Scenarios of the CMS Experiment, CMS Conference Report 2003-007

[29] R. Brun, F. Rademakers, ROOT - An Object Oriented Data Analysis Framework, Nucl. Instr. and Methods A 389 (1997) 81.

[30] Full description of the Honeywell HIH-3610 Series sensors can be found in: http://content.honeywell.com/sensing/prodinfo/humiditymoisture/

[31] G. Cervelli, *et al.*, A radiation tolerant laser driver array for optical transmission in the LHC experiments, CERN-2001-005, September 2001, pp. 155.

[32] S. Dris, M. Axer, K. Gill, R. Grabit, R. Macias, E. Noah, J. Troska and F. Vasey, Predicting the In-System Performance of the CMS Tracker Analog Readout Optical Links, Proceedings of the 10^{th} Workshop on Electronics for LHC experiments, CERN-LHCC-2004-030

[33] H. Bichsel, Rev. Mod. Phys. 60, 663 (1988)

[34] A. Macchiolo, Results of Laboratory Measurements on IB2 CMS Silicon Sensors, Private communication, (2007).

[35] M.T. Brunetti *et al.*, Electrical Qualification of the preproduction of Analogue Opto-Hybrid Circuits for the CMS Tracker Inner Barrel and Inner Disks, CMS NOTE 2003/027

[36] ST Microelectronics, I-95021 Catania, Italy.

[37] CAEN S.p.A. Via Vetraia, 11 I-55049 Viareggio (LU), Italy

[38] LABEN S.p.A. S.S. Padana Superiore, 290 I-20090 Vimodrone (MI), Italy